ResearchGate

See discussions, stats, and author profiles for this publication at: https://www.researchgate.net/publication/343444931

An isogeometric mixed thin-shell formulation for multi-patch analyses in the framework of non-linear elasticity

Preprint · August 2020

CITATIONS
0

READS
150

3 authors:

Yujie Guo
Nanjing University of Aeronautics & Astronautics
17 PUBLICATIONS **264** CITATIONS
SEE PROFILE

Zhihui Zou
Brigham Young University - Provo Main Campus
6 PUBLICATIONS **15** CITATIONS
SEE PROFILE

Martin Ruess
Hochschule Düsseldorf
57 PUBLICATIONS **1,428** CITATIONS
SEE PROFILE

All content following this page was uploaded by Martin Ruess on 05 August 2020.

The user has requested enhancement of the downloaded file.

An isogeometric mixed thin-shell formulation for multi-patch analyses in the framework of non-linear elasticity

Yujie Guo[a,*], Zhihui Zou[b], Martin Ruess[c]

[a]*Interdisciplinary Research Institute of Aeronautics and Astronautics, College of Aerospace Engineering, Nanjing University of Aeronautics and Astronautics, 210016, Nanjing, P. R. China.*
[b]*Department of Civil and Environmental Engineering, Brigham Young University, USA*
[c]*Department of Mechanical and Process Engineering, Düsseldorf University of Applied Sciences, Germany*

Abstract

In continuation of a membrane locking-free isogeometric thin-shell formulation for linear analyses, this contribution introduces an extension to large displacements in combination with a continuity preserving coupling scheme for multi-patch NURBS models. The latter bears some immanent challenges of CAD-derived designs including arbitrary trimmed geometries, non-conforming patch discretizations and overlapping domains. We address all of them herein and follow a Hellinger-Reissner mixed formulation to regain full control over membrane locking effects. We extend the variational formulation consistently following the fundamental aspects of a weighted residual approach to enforce weakly the interface conditions among coupled patches and utilize the finite cell method to handle properly the issue of trimming. We critically assess the performance of the proposed method studying several numerical examples of linear and non-linear elasticity. We compare our method with established developments in this field and demonstrate superior achievements with regard to solution quality, robustness and computational complexity.

Keywords: Hellinger-Reissner, Kirchhoff-Love shell, Nitsche-type coupling, patch trimming, membrane locking

*Corresponding author;
Yujie Guo, College of Aerospace Engineering, Nanjing University of Aeronautics and Astronautics, 210016, Nanjing, P.R. China; E-mail: yujieguo@nuaa.edu.cn, yujie.guo8604@gmail.com

Preprint

Contents

1. Introduction

In a broader sense, isogeometric and thin-shell modeling form a rewarding symbiotic relationship. Both methods share an immanent surface-based model description in combination with the potential of and the need for higher order approximation and continuity properties [1, 2].

Pure displacement-based shell formulations are well known to be prone to various locking phenomena [3], thus responding overly stiff to loading, when indicated. Methods following the *Assumed/Enhanced Natural Strain* idea rectify the usual shortcomings of insufficient interpolation capabilities in the context of locking as well as mixed formulations do [4–6], currently providing a number of efficient and accurate strategies for solid shell elements [7–10].

In the context of thin-shell analysis, it is the distinct imbalance in the ratio of membrane to bending stiffness which may lead to membrane locking, substantially compromising the overall deformation performance [11, 12]. Mixed formulations following the principle of *Hellinger & Reissner* [13, 14] and variants thereof are established two-field concepts which naturally counteract membrane locking through an independent consideration of displacement and stress quantities [15]. Moreover, in the context of non-linear shell analysis several studies have repeatedly confirmed a superior numerical behavior of mixed formulations over pure single-field formulations allowing for significantly larger step sizes and less iterations to regain equilibrium of the governing balance equations. Recently, *Magisano et al.* have demonstrated a signifant quality and performance jump in the framework of Koiter's asymptotic method [16] and an extended Koiter-Newton path-following method [17] to predict the post-buckling response of slender structures. Moreover, in [18] they introduced a highly efficient mixed integration point approach based on the Hellinger-Reissner principle outperforming pure displacement-based formulations in terms of accuracy and robustness. Their proposed strategy is naturally confined to element level, thus, being a convincing two-field enrichment method with positive impact in Newton-based solution schemes.

In the framework of isogeometric analysis (IGA), mixed thin-shell formulations first found attention with the work of *Echter* [19] who presented a displacement-stress formulation based on the Hellinger-Reissner variational principle in order to remove in-plane locking effects in linear shell analysis. Just recently, a novel mixed approach was introduced in [20] which uses a pure $\mathcal{H}^1$ space for interpolation, hence allowing for a successful $\mathcal{C}^0$-continuous coupling of patches though being restricted to conforming discretizations. The indispensable need for coupling along arbitrary interfaces of patches and even overlapping domains as common in CAD-derived NURBS models still is a limiting factor in isogeometric analysis. Despite a number of advancements which have been made in recent years [21–27], the general applicability of isogeometric analysis to arbitrary multi-patch shell structures widely shows a number of improvable aspects. Three major strategies are currently the established standard in isogeometric patch coupling methods including (i) penalty methods [28–30], (ii) Lagrange multiplier and augmented Lagrange multiplier methods [31, 32] and (iii) Nitsche-like methods [22, 24, 33–37]. A good overview and comparison of these coupling strategies was recently gathered by *Apostolatos et al.* [23].

Herein, we propose two major extensions to the actual state in isogeometric thin-shell analysis to relax the currently tight field of modeling capabilities to a general approach:

1. We extend the Hellinger-Reissner formulation of [11] to a large deformation analysis the-

ory, thus obtaining a locking-free isogeometric thin-shell formulation. Furthermore, we embed the implementation of the new shell element into a fictitious-domain extended analysis framework to allow for a straightforward treatment of trimmed and/or overlapping NURBS domains. The fictitious domain approach follows the basic principles of the finite cell method which we have introduced in earlier publications [22, 34, 38, 39]. For general details on the finite cell method we refer the reader to [40–42]. The specialization of the approach to thin-shell NURBS analysis can be found in detail in [24, 39]. Herein, we provide a brief summary of the basic principles of the method in order to ensure contextual consistency.

2. We extend our mixed formulation to a variationally consistent formulation for the weak enforcement of coupling constraints. We have demonstrated in [22, 38] the performance gain and the benefits of this approach for large deformation thin-shell analysis in the framework of a pure displacement-based Kirchhoff-Love theory. The basic idea traces back to a formulation introduce by *J.A. Nitsche* [43] for the enforcement of essential boundary conditions in Laplace problems and has been re-visited and studied in depth since then in a number of seminal papers by *Hansbo et al.* [44, 45], *Becker et al.* [46] and *Embar et al.* [47] to mention a few. The method obtained another push with the advent of isogeometric methods by a number of contributions in the fields of elastictiy [36, 37, 48] and fluid-structure interaction [49–51].

Both, the non-linear shell formulation of the Hellinger-Reissner model proposed in [11] and its extension to enforce weakly coupling constraints along arbitrary domain interfaces mark an important step forward in the context of isogeometric thin-shell analysis of CAD derived geometries of industrial relevance. We study critically the novel aspects introduced in the formulation and demonstrate the method's performance with a number of benchmark problems and examples which demonstrate the applicability and relevance for engineering problems.

The manuscript has the following structure: in section 2 we provide a brief summary of the relevant shell theory fundamentals which are necessary to introduce our extension. In section 3 we introduce stepwise the Nitsche extensions for a variationally consistent patch coupling. Moreover, we address the integration along trimming curves and aspects of stabilization which has relevance in the current formulation. In section 4, we test our method and carefully study various performance aspects to reveal the method's capabilities and potential limitations. Finally, we summarize the main aspects and findings and draw conclusions in section 5.

2. The Hellinger-Reissner extended KL shell formulation

In this section, we start with a concise representation of the Kirchhoff-Love shell formulation, limited to the extent that is necessary to introduce the Hellinger-Reissner principles in the context of large deformation analysis. Herein, we also provide the discrete formulation which we implemented in our isogeometric analysis framework. Moreover, we review concisely the basic idea of the finite cell method as applied in isogeometric analysis to tackle the problem of trimmed shell patches. An elaborate presentation of the method is given in [40] for general structures and in [22] tailored to suit thin-shell analysis.

Notation: In the following, we use an upper case notation for quantities which refer to the undeformed reference configuration, and a lower case notation for quantities which refer to the current deformed configuration. Without specific notation, Greek indices take values $\{1, 2\}$ and Latin indices take values $\{1, 2, 3\}$.

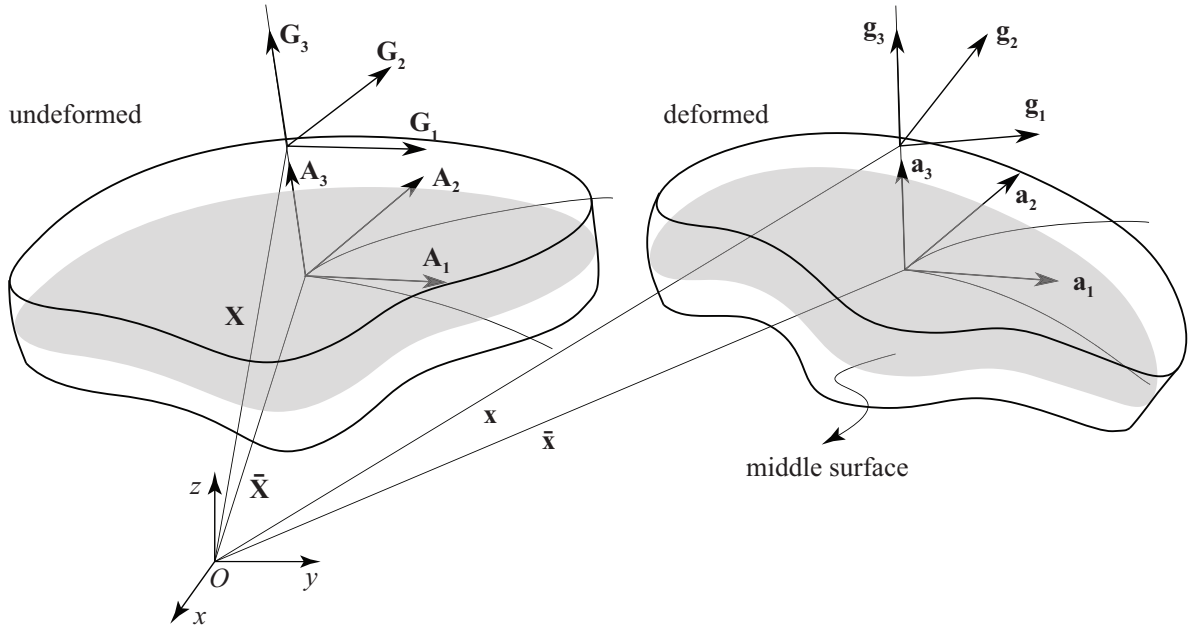

Figure 1: Schematics of the shell kinematics.

2.1. Shell kinematics

The reference and current configurations of a shell-like body, as illustrated in Figure 1, are parameterized as

$$\mathbf{X}(\xi_1, \xi_2, \xi_3) = \bar{\mathbf{X}}(\xi_1, \xi_2) + \xi_3 \, \mathbf{D}(\xi_1, \xi_2), \tag{1}$$

$$\mathbf{x}(\xi_1, \xi_2, \xi_3) = \bar{\mathbf{x}}(\xi_1, \xi_2) + \xi_3 \, \mathbf{d}(\xi_1, \xi_2) \tag{2}$$

where $\bar{\mathbf{X}}$ and $\bar{\mathbf{x}}$ denote the shell middle surface, where $\mathbf{D}$ and $\mathbf{d}$ denote the directors of the shell in the reference and current configurations, respectively, and where $\xi_3 \in [-0.5\,h, 0.5\,h]$ varies linearly through the shell thickness h. For conciseness, we omit the parametric coordinate ξ_i in the following.

The base vectors of the shell mid-surface are defined as:

$$\mathbf{A}_\alpha = \bar{\mathbf{X}}_{,\alpha}, \quad \mathbf{A}_3 = \mathbf{D} = \frac{\mathbf{A}_1 \times \mathbf{A}_2}{|\mathbf{A}_1 \times \mathbf{A}_2|}, \tag{3}$$

$$\mathbf{a}_\alpha = \bar{\mathbf{x}}_{,\alpha}, \quad \mathbf{a}_3 = \mathbf{d}\,. \tag{4}$$

where $(\cdot)_{,\alpha}$ denotes the partial derivative $\partial(\cdot)/\partial\xi_\alpha$. With (3) and (4), the covariant base vectors at any point in the shell continuum are:

$$\mathbf{G}_\alpha = \mathbf{X}_{,\alpha} = \bar{\mathbf{X}}_{,\alpha} + \xi_3\,\mathbf{D}_{,\alpha} = \mathbf{A}_\alpha + \xi_3\,\mathbf{D}_{,\alpha} \qquad \mathbf{G}_3 = \mathbf{X}_{,3} = \mathbf{D}, \tag{5}$$

$$\mathbf{g}_\alpha = \mathbf{x}_{,\alpha} = \bar{\mathbf{x}}_{,\alpha} + \xi_3\,\mathbf{d}_{,\alpha} = \mathbf{a}_\alpha + \xi_3\,\mathbf{d}_{,\alpha} \qquad \mathbf{g}_3 = \mathbf{x}_{,3} = \mathbf{d} \tag{6}$$

which allows to express the Green-Lagrange strain tensor $\mathbf{E}$ as:

$$\mathbf{E} = E_{ij}\,\mathbf{G}^i \otimes \mathbf{G}^j = \frac{1}{2}\left(\mathbf{F}^{\mathrm{T}}\mathbf{F} - \mathbf{I}\right) \tag{7}$$

where $\mathbf{F} = \mathrm{d}\mathbf{x}/\mathrm{d}\mathbf{X}$ is the material deformation gradient, $\mathbf{I}$ is the identity tensor and the strain tensor coefficients are:

$$E_{ij} = \frac{1}{2}(g_{ij} - G_{ij}) \tag{8}$$

where

$$g_{ij} = \mathbf{g}_i \cdot \mathbf{g}_j, \quad G_{ij} = \mathbf{G}_i \cdot \mathbf{G}_j. \tag{9}$$

Substituting (5) and (6) into (8), the Green-Lagrange strain coefficients have the form:

$$E_{\alpha\beta} = \frac{1}{2}\left[(\mathbf{a}_\alpha \cdot \mathbf{a}_\beta + \xi_3\mathbf{a}_\alpha \cdot \mathbf{d}_{,\beta} + \xi_3\mathbf{d}_{,\alpha} \cdot \mathbf{a}_\beta) - (\mathbf{A}_\alpha \cdot \mathbf{A}_\beta + \xi_3\mathbf{A}_\alpha \cdot \mathbf{D}_{,\beta} + \xi_3\mathbf{D}_{,\alpha} \cdot \mathbf{A}_\beta)\right] \tag{10}$$

$$E_{\alpha 3} = \frac{1}{2}\left(\mathbf{a}_\alpha \cdot \mathbf{d} + \xi_3\mathbf{d}_{,\alpha} \cdot \mathbf{d} - \mathbf{A}_\alpha \cdot \mathbf{D} - \xi_3\mathbf{D}_{,\alpha} \cdot \mathbf{D}\right) \tag{11}$$

$$E_{33} = \frac{1}{2}\left(\mathbf{d} \cdot \mathbf{d} - \mathbf{D} \cdot \mathbf{D}\right)\ . \tag{12}$$

The inextensibility assumption of the director, i.e. $|\mathbf{d}| = 1$, leads to

$$\mathbf{d} \cdot \mathbf{d} = \mathbf{D} \cdot \mathbf{D} = 1, \tag{13}$$

$$\mathbf{d}_{,\alpha} \cdot \mathbf{d} = \mathbf{D}_{,\alpha} \cdot \mathbf{D} = 0 \tag{14}$$

and according to the definition of $\mathbf{D}$ we find that $\mathbf{A}_\alpha \cdot \mathbf{D} = 0$ and $\mathbf{A}_\alpha \cdot \mathbf{D}_{,\beta} = -\mathbf{D} \cdot \mathbf{A}_{\alpha,\beta} = \mathbf{D}_{,\alpha} \cdot \mathbf{A}_\beta$, where $\mathbf{A}_{\alpha,\beta} = \bar{\mathbf{X}}_{,\alpha\beta}$. Therefore, (10) to (12) become

$$E_{\alpha\beta} = \frac{1}{2}\left[(\mathbf{a}_\alpha \cdot \mathbf{a}_\beta - \mathbf{A}_\alpha \cdot \mathbf{A}_\beta) + \xi_3\left(\mathbf{a}_\alpha \cdot \mathbf{d}_{,\beta} + \mathbf{d}_{,\alpha} \cdot \mathbf{a}_\beta + 2\mathbf{A}_{\alpha,\beta} \cdot \mathbf{D}\right)\right] \tag{15}$$

$$E_{\alpha 3} = \frac{1}{2}\mathbf{a}_\alpha \cdot \mathbf{d} \tag{16}$$

$$E_{33} = 0\ . \tag{17}$$

The Kirchhoff-Love theory assumes the current director to be perpendicular to the middle surface, thus defining:

$$\mathbf{d} = \frac{\mathbf{a}_1 \times \mathbf{a}_2}{|\mathbf{a}_1 \times \mathbf{a}_2|}\ . \tag{18}$$

which simplifies equations (15) to (17) to:

$$\begin{aligned} E_{\alpha\beta} &= \frac{1}{2}\left[(\mathbf{a}_\alpha \cdot \mathbf{a}_\beta - \mathbf{A}_\alpha \cdot \mathbf{A}_\beta) + 2\,\xi_3\,(\mathbf{A}_{\alpha,\beta} \cdot \mathbf{D} - \mathbf{a}_{\alpha,\beta} \cdot \mathbf{d})\right] \\ &= \varepsilon_{\alpha\beta} + \xi_3\,\kappa_{\alpha\beta} \qquad (19) \\ E_{\alpha 3} &= E_{33} = 0 \qquad (20) \end{aligned}$$

where the membrane strain $\varepsilon_{\alpha\beta}$ and bending strain $\kappa_{\alpha\beta}$ are defined as:

$$\begin{aligned} \varepsilon_{\alpha\beta} &= \frac{1}{2}(\mathbf{a}_\alpha \cdot \mathbf{a}_\beta - \mathbf{A}_\alpha \cdot \mathbf{A}_\beta) \qquad (21) \\ \kappa_{\alpha\beta} &= \mathbf{A}_{\alpha,\beta} \cdot \mathbf{D} - \mathbf{a}_{\alpha,\beta} \cdot \mathbf{d}\ . \qquad (22) \end{aligned}$$

2.2. Variational formulation and linearization

For non-linear elastic problems, the Hellinger-Reissner variational formulation provides the following expression for the potential energy of the shell:

$$\begin{aligned} \mathcal{W}(\mathbf{u}, \tilde{\mathbf{E}}) &= \mathcal{W}_I(\mathbf{u}, \tilde{\mathbf{E}}) + \mathcal{W}_E(\mathbf{u}) \\ &= \int_\Omega \left(\tilde{\mathbf{E}} : \mathbf{C} : \mathbf{E} - \frac{1}{2}\,\tilde{\mathbf{E}} : \mathbf{C} : \tilde{\mathbf{E}}\right) d\Omega - \lambda \left[\int_\Omega \mathbf{p}_0 \cdot \mathbf{u}\, d\Omega + \int_{\Gamma_t} \mathbf{t}_0 \cdot \mathbf{u}\, d\Gamma\right] \qquad (23) \end{aligned}$$

where $\mathcal{W}_I$ and $\mathcal{W}_E$ are the internal and external energy, respectively, where $\mathbf{u}$ and $\tilde{\mathbf{E}}$ are the unknown displacement and strain variables, respectively, where $\mathbf{E}$ is the Green-Lagrange strain defined in (15) to (17), $\mathbf{C}$ is the elasticity matrix defined in the curvilinear coordinate system, where λ is the applied load factor, $\mathbf{p}_0$ is the unit surface load on the domain Ω and $\mathbf{t}_0$ is the unit traction along the Neumann boundary Γ_t. For simplicity, we assume that $\mathbf{p}_0$ and $\mathbf{t}_0$ are dead loads which are independent of the body deformation.

To counteract membrane locking, the assumed strain $\tilde{\mathbf{E}}$ is defined as:

$$\tilde{\mathbf{E}} = \tilde{\boldsymbol{\varepsilon}} + \xi_3\,\boldsymbol{\kappa} \qquad (24)$$

where $\boldsymbol{\kappa}$ is the standard bending strain whose components are defined in (22), where $\tilde{\boldsymbol{\varepsilon}}$ is the independently defined assumed membrane strain.

Substitution of equations (24) and (19) into (23) and utilizing the pre-integration along the thickness direction leads to:

$$\mathcal{W}(\mathbf{u}, \tilde{\boldsymbol{\varepsilon}}) = h \int_{\Omega_0} \tilde{\boldsymbol{\varepsilon}} : \mathbf{C} : \left(\boldsymbol{\varepsilon} - \frac{1}{2}\,\tilde{\boldsymbol{\varepsilon}}\right) \mathrm{d}\Omega + \frac{h^3}{12} \int_{\Omega_0} \boldsymbol{\kappa} : \mathbf{C} : \boldsymbol{\kappa}\, \mathrm{d}\Omega + \mathcal{W}_E(\mathbf{u}) \qquad (25)$$

where $\boldsymbol{\varepsilon}$ is the membrane strain tensor with components defined in (21) and where Ω_0 is the shell's reference surface, e.g. the middle surface.
Invoking the stationary condition $\delta\mathcal{W} = 0$ of the energy functional (25) results in:

$$\delta\mathcal{W}(\delta\mathbf{u}, \delta\tilde{\boldsymbol{\varepsilon}}) = \delta\mathcal{W}_I(\delta\mathbf{u}, \delta\tilde{\boldsymbol{\varepsilon}}) + \delta\mathcal{W}_E(\delta\mathbf{u})$$

$$= \; h \int_{\Omega_0} (\delta\tilde{\boldsymbol{\varepsilon}} : \mathbf{C} : \boldsymbol{\varepsilon} + \tilde{\boldsymbol{\varepsilon}} : \mathbf{C} : \delta\boldsymbol{\varepsilon} - \tilde{\boldsymbol{\varepsilon}} : \mathbf{C} : \delta\tilde{\boldsymbol{\varepsilon}}) \, \mathrm{d}\Omega$$

$$+ \; \frac{h^3}{12} \int_{\Omega_0} \boldsymbol{\kappa} : \mathbf{C} : \delta\boldsymbol{\kappa} \, \mathrm{d}\Omega - \lambda \left[\int_{\Omega_0} \mathbf{p}_0 \cdot \delta\mathbf{u} \, \mathrm{d}\Omega + \int_{\Gamma_t} \mathbf{t}_0 \cdot \delta\mathbf{u} \, \mathrm{d}\Gamma \right] = 0 \quad (26)$$

where $\delta\boldsymbol{\varepsilon}$, $\delta\tilde{\boldsymbol{\varepsilon}}$ and $\delta\boldsymbol{\kappa}$ denote the variation of the membrane strain, assumed membrane strain and bending strain, respectively.

2.3. Discretization

Following the concept of isogeometric analysis, the displacement field $\mathbf{u}$ and its variations $\delta\mathbf{u}$ are discretized using the NURBS basis functions of the geometric model description, which reads:

$$\mathbf{u} \;\approx\; \sum_{k=1}^{n} R_k^{p,q} \, \mathbf{U}_k \;=\; \mathbf{R}^{\mathrm{T}}\mathbf{U} \quad (27)$$

$$\delta\mathbf{u} \;\approx\; \sum_{k=1}^{n} R_k \, \delta\mathbf{U}_k \;=\; \mathbf{R}^{\mathrm{T}} \, \delta\mathbf{U} \quad (28)$$

where $\mathbf{U}_k$ and $R_k^{p,q}$ are the k-th displacement variables and NURBS basis with orders p and q in ξ_1 and ξ_2 directions, respectively, where $\mathbf{R}$ and $\mathbf{U}$ are the vectors collecting the corresponding quantities.

The independent assumed membrane strain components are interpolated by three lower order bases $\tilde{R}_A^{p-1,q}$, $\tilde{R}_B^{p,q-1}$ and $\tilde{R}_C^{p-1,q-1}$ as, cf. [19]:

$$\tilde{\boldsymbol{\varepsilon}} \;=\; \begin{bmatrix} \tilde{\varepsilon}_{11} \\ \tilde{\varepsilon}_{22} \\ 2\,\tilde{\varepsilon}_{12} \end{bmatrix} \;\approx\; \begin{bmatrix} \sum_{A=1}^{m} \tilde{R}_A^{p-1,q} (\tilde{\epsilon}_{11})_A \\ \sum_{B=1}^{s} \tilde{R}_B^{p,q-1} (\tilde{\epsilon}_{22})_B \\ \sum_{C=1}^{l} \tilde{R}_C^{p-1,q-1} (2\,\tilde{\epsilon}_{12})_C \end{bmatrix} \;=\; \tilde{\mathbf{R}}^{\mathrm{T}} \tilde{\boldsymbol{\epsilon}} \quad (29)$$

where $(\tilde{\epsilon}_{11})_A$, $(\tilde{\epsilon}_{22})_B$ and $(2\,\tilde{\epsilon}_{12})_C$ are the assumed membrane strain variables at each control point, where $\tilde{\mathbf{R}}^{\mathrm{T}}$ and $\tilde{\boldsymbol{\epsilon}}$ are the matrices collecting the corresponding quantities. The same holds for the variations $\delta\tilde{\boldsymbol{\varepsilon}}$.

The NURBS basis $\tilde{R}_A^{p-1,q}$ in (29) uses functions of order $(p-1)$ and q in the ξ_1 and ξ_2 directions, respectively, which lowers the continuity of the corresponding assumed membrane strain $\tilde{\varepsilon}_{11}$ in the ξ_1 direction and maintains the highest continuity in the ξ_2 direction. Similar operations are adopted for the discretizations of $\tilde{\varepsilon}_{22}$ and $2\,\tilde{\varepsilon}_{12}$. It is worth to note that we use the same number of elements for the discretizations of $\mathbf{u}$ and $\tilde{\boldsymbol{\varepsilon}}$, which results in a different number of control points for the unknown variables.

Substituting (27), (28) and (29) into the governing equations (26) provides the discrete equilibrium equations:

$$\mathbf{G}(\mathbf{U}, \tilde{\boldsymbol{\epsilon}}, \lambda) \;=\; \mathbf{f}_I(\mathbf{U}, \tilde{\boldsymbol{\epsilon}}) - \lambda \mathbf{f}_E \;=\; \mathbf{0} \quad (30)$$

where $\mathbf{G}(\mathbf{U}, \tilde{\boldsymbol{\epsilon}}, \lambda)$ represents the residual between the internal force vector $\mathbf{f}_I(\mathbf{U}, \tilde{\boldsymbol{\epsilon}})$ and the external force vector $\mathbf{f}_E$, with:

$$\mathbf{f}_I(\mathbf{U}, \tilde{\boldsymbol{\epsilon}}) = \int_{\Omega_0} \left(\frac{\partial \tilde{\mathbf{N}}}{\partial \tilde{\boldsymbol{\epsilon}}} : \boldsymbol{\varepsilon} + \tilde{\mathbf{N}} : \frac{\partial \boldsymbol{\varepsilon}}{\partial \mathbf{U}} - \tilde{\mathbf{N}} : \frac{\partial \tilde{\boldsymbol{\varepsilon}}}{\partial \tilde{\boldsymbol{\epsilon}}} + \mathbf{M} : \frac{\partial \boldsymbol{\kappa}}{\partial \mathbf{U}} \right) \mathrm{d}\Omega \tag{31}$$

$$\mathbf{f}_E = \int_{\Omega_0} \mathbf{p}_0 \cdot \frac{\partial \mathbf{u}}{\partial \mathbf{U}} \, \mathrm{d}\Omega + \int_{\Gamma_t} \mathbf{t}_0 \cdot \frac{\partial \mathbf{u}}{\partial \mathbf{U}} \, \mathrm{d}\Gamma \tag{32}$$

where $\tilde{\mathbf{N}}$ and $\mathbf{M}$ are the stress resultant and bending moment tensors defined in the contravariant basis of the middle surface [52]. Assuming the St. Venant-Kirchhoff constitutive model, they relate to the membrane and bending strain, component-wise, by the relations:

$$\tilde{N}^{\alpha\beta} = h \, C^{\alpha\beta\gamma\delta} \, \tilde{\varepsilon}_{\gamma\delta} \tag{33}$$

$$M^{\alpha\beta} = \frac{h^3}{12} \, C^{\alpha\beta\gamma\delta} \, \kappa_{\gamma\delta} \, . \tag{34}$$

In general, equation (30) is non-linear in terms of $\mathbf{U}$ and $\tilde{\boldsymbol{\epsilon}}$ and is used in linearized form which leads to the tangent stiffness matrix:

$$\mathbf{K}_T = \int_{\Omega_0} \left(\frac{\partial \tilde{\mathbf{N}}}{\partial \tilde{\boldsymbol{\epsilon}}} : \frac{\partial \boldsymbol{\varepsilon}}{\partial \mathbf{U}} + \left[\frac{\partial \tilde{\mathbf{N}}}{\partial \tilde{\boldsymbol{\epsilon}}} : \frac{\partial \boldsymbol{\varepsilon}}{\partial \mathbf{U}} \right]^{\mathrm{T}} + \tilde{\mathbf{N}} : \frac{\partial^2 \boldsymbol{\varepsilon}}{\partial \mathbf{U} \partial \mathbf{U}} - \frac{\partial \tilde{\mathbf{N}}}{\partial \tilde{\boldsymbol{\epsilon}}} : \frac{\partial \tilde{\boldsymbol{\varepsilon}}}{\partial \tilde{\boldsymbol{\epsilon}}} + \frac{\partial \mathbf{M}}{\partial \mathbf{U}} : \frac{\partial \boldsymbol{\kappa}}{\partial \mathbf{U}} + \mathbf{M} : \frac{\partial^2 \boldsymbol{\kappa}}{\partial \mathbf{U} \partial \mathbf{U}} \right) \mathrm{d}\Omega \, . \tag{35}$$

The equilibrium equation (30) is solved in an iterative process using the linearization until the residual is reduced to a desired tolerance.

For linear elastic problems, the tangent stiffness matrix further simplifies to:

$$\mathbf{K}_T^L = \int_{\Omega_0} \left(\frac{\partial \tilde{\mathbf{N}}}{\partial \tilde{\boldsymbol{\epsilon}}} : \frac{\partial \boldsymbol{\varepsilon}}{\partial \mathbf{U}} + \left[\frac{\partial \tilde{\mathbf{N}}}{\partial \tilde{\boldsymbol{\epsilon}}} : \frac{\partial \boldsymbol{\varepsilon}}{\partial \mathbf{U}} \right]^{\mathrm{T}} - \frac{\partial \tilde{\mathbf{N}}}{\partial \tilde{\boldsymbol{\epsilon}}} : \frac{\partial \tilde{\boldsymbol{\varepsilon}}}{\partial \tilde{\boldsymbol{\epsilon}}} + \frac{\partial \mathbf{M}}{\partial \mathbf{U}} : \frac{\partial \boldsymbol{\kappa}}{\partial \mathbf{U}} \right) \mathrm{d}\Omega \, . \tag{36}$$

2.4. Tackling the challenge of trimming

Trimming provides a simple mechanism in the design process of complex geometries in CAD systems. It employs Boolean operations between objects, thus allowing for an arbitrary pruning of the geometry. Shell structures which are modeled by NURBS surfaces are trimmed by a set of trimming curves which are independent of the underlying parametric space of the NURBS representation. Hence, a direct analysis of the trimmed shell model is not possible without further effort to establish a link between the NURBS patch and the independent trimming curve, cf. Figure 2. A detailled overview of the trimming technology, the challenges with regard to an isogeometric analysis and the current solution strategies were elaborated intensively by *Marrusig & Hughes* [53].

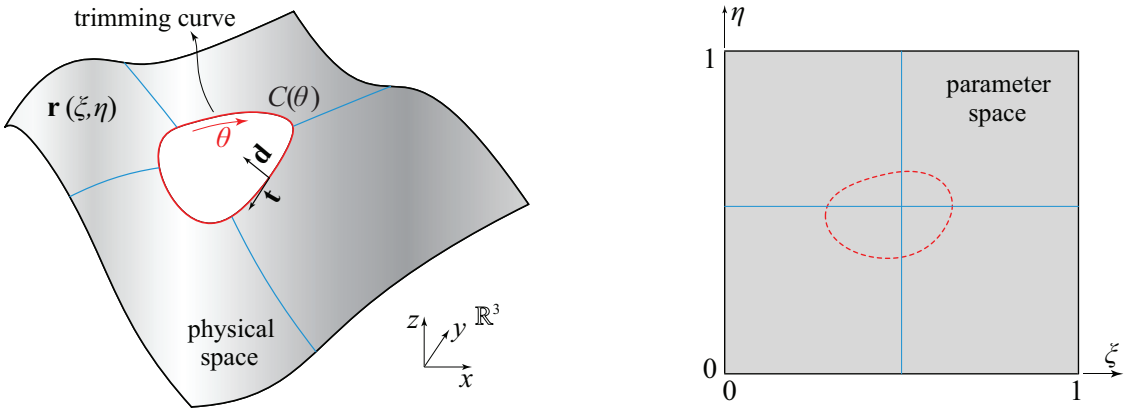

(a) trimmed geometry (b) parametric space

Figure 2: (a) NURBS surface patch with trimming curve representing the shell mid-surface definition, (b) corresponding parametric space.

Besides a number of strategies to handle trimming including seminal works on local reconstruction methods [28, 54–56], sub-division surface methods [57–59] or T-splines [60, 61] to mention a few, the idea of a fictitious domain extension to consider trimmed areas without contribution to the physical problem has gained much attention [40, 41]. It is primarily the simplicity of the fictitious domain approach which substantiates its popularity in the context of trimmed NURBS domains. The fictitious domain idea, considered herein, is based on the principles of the finite cell method introduced by *Parvizian et al.* [42] and was later adapted to the framework of isogeometric analysis by *Schillinger & Ruess* [48, 62].

The overall idea of the method is based on a penalization of the stresses and forces in fictitious sub-domains such that their contribution to the total potential energy is confined to a negligible contribution. In the context of isogeometric analysis, any trimmed region is considered to be a fictitious sub-domain. Hence, consideration of trimming essentially reduces to the process of a refined numerical integration scheme of the variational formulation which is capable to distinguish between the physical domain and the penalized fictitious domain. Herein, the integrals (31) and (32) of the balance equation (30) are defined over the actual analysis domain, in general using trimmed NURBS patches to represent the shell mid-surface. The strategic approach to evaluate the integrals on element level has impact on the overall assembly performance. The ideal case of an algorithmic simple and numerically cheap but exact integration is still an open issue though a number of sophisticated methods have been developed or adapted and refined from other fields of simulation. Most of them can be classified either as algorithmic simple or numerically cheap or geometrically exact. The proposed strategies include local triangulation schemes to define the integration sub-domains [54, 63], in a more refined variant by considering the exact boundary description using a blending function approach [64], or using tailored integration schemes which involve a pre-computation of the quadrature point location to fit best possible the integration do-

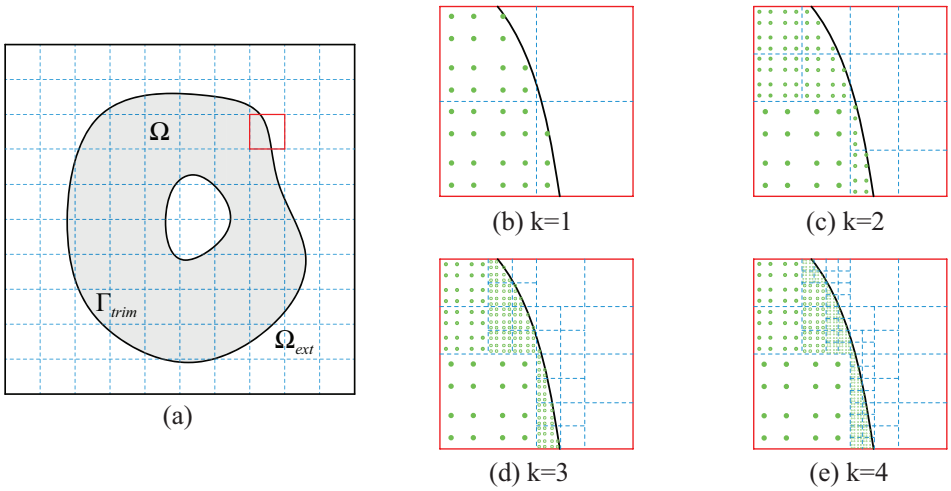

Figure 3: Adaptive quadrature based on recursive bi-section: (a) original embedded domain, (b)-(e) generation of a quad-tree and corresponding integration points from tree depth $k = 1$ to $k = 4$.

main [65]. For an exhaustive overview and detailed survey of suitable integration methods, we refer to [53].

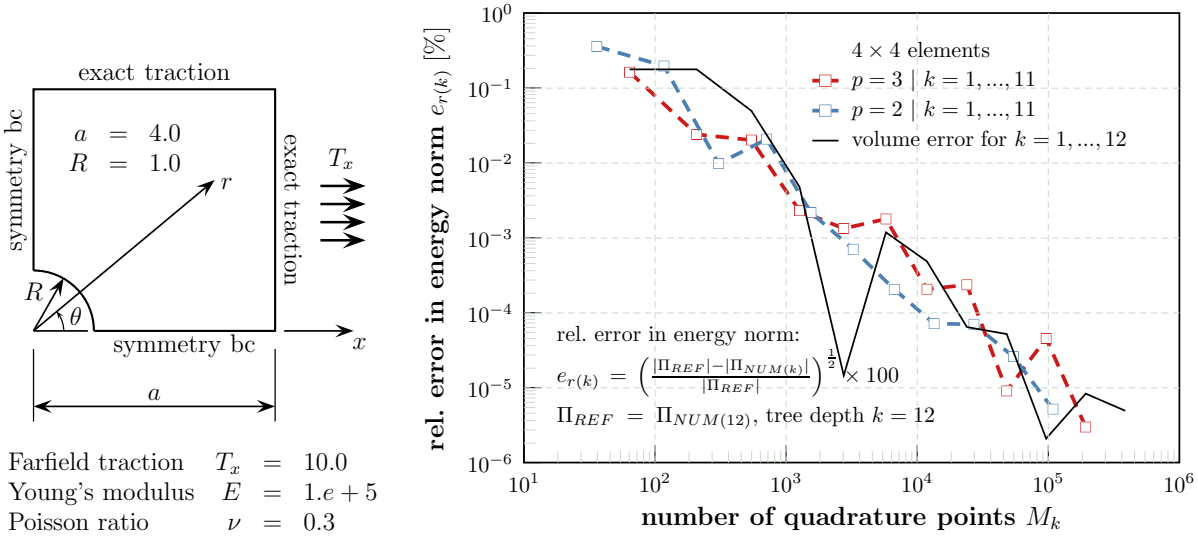

Figure 4: Impact of the tree depth on the analysis performance: (a) test example, documented in detail in [36, 66], (b) relative change of the error in energy norm for increasing tree depth k.

In our analysis framework, we favor an adaptive quadrature scheme as illustrated in Figure 3. Based in a recursive bi-section, cut elements are sub-divided to obtain a composed integration domain which approximates the relevant sectors by a tree-like hierarchy of adaptive sub-cells. Full integration order is used for each sub-cell, thus concentrating quadrature points towards the cutting interface. A location function $\alpha(\mathbf{x})$ is used to penalize the stress resultants and bending moments

of the variational formulation with $\alpha = 1$ for all points in the physical domain and $\alpha \ll 1$ for points of the fictitious domain. The mehtod allows for a smooth extension of the solution into the fictitious domain and ensures higher-order accuracy [62]. The accuracy of the integration is controlled by the tree depth k. The influence of k on the overall solution quality is illustrated with the example of an infinite plate with a circular hole under constant in-plane tension, depicted in Figure 4. We analysed the problem in a different context and with different focus in [36] to which we refer the reader for all details. The graph in Figure 4 reveals the influence of the tree depth on the accuracy of the analysis result. The relative error in energy norm reduces linearly with increasing tree depth k, referred to a reference value which was computed for $k = 12$. The linear degression of the volume error at a similar rate confirmed a linear dependency of the accuracy level on the sub-cell resolution of the trimmed domain.

3. Weak enforcement of coupling constraints between trimmed shell patches

Nitsche's method favors a weak enforcement of constraints in the equilibrium equation (26) by consideration of the constraints in terms of weighted residuals. The extended governing equilibrium equations are variationally consistent but require stabilization in some cases, to ensure ellipticity of the bi-linear form of (26).
In the following, we introduce the corresponding terms for a coupling of shell patches following the Hellinger-Reissner formulation introduced in the previous section 2. Then, we briefly discuss aspects of their isogeometric discretization. Finally, we discuss the integration of the coupling terms and the estimation of suitable element-wise stabilization parameters.

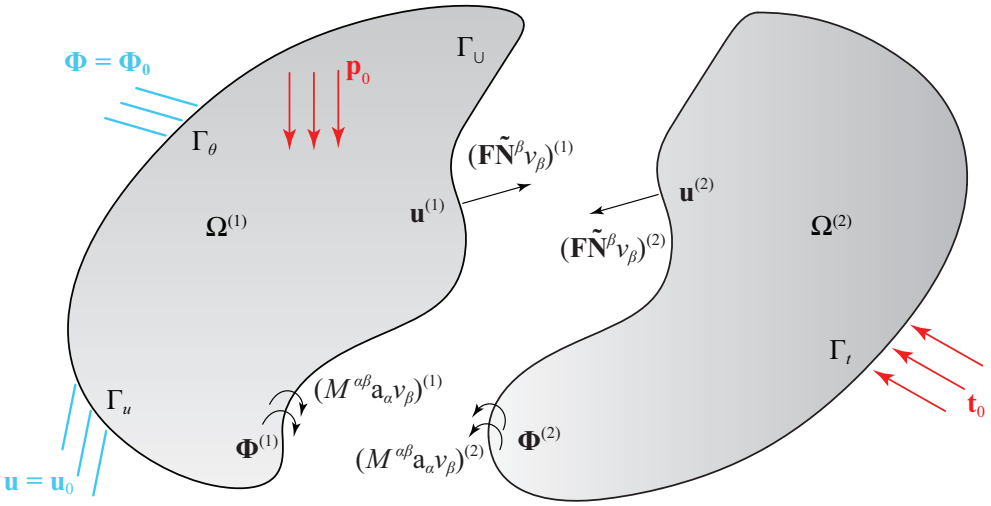

Figure 5: Schematic representation of shell coupling problems.

3.1. Variationally consistent coupling extension

The coupling between shell patches can be viewed as an interface problem where the following displacement continuity and force compatibility conditions at the mutual boundary must be

ensured during deformation, cf. Figure 5:

$$\mathbf{u}^{(1)} - \mathbf{u}^{(2)} = \mathbf{0} \quad \text{on } \Gamma_{\cup} \tag{37}$$

$$\mathbf{\Phi}^{(1)} - \mathbf{\Phi}^{(2)} = \mathbf{0} \quad \text{on } \Gamma_{\cup} \tag{38}$$

$$\left(\mathbf{F}\tilde{\mathbf{N}}^{\beta}\,\nu_{\beta}\right)^{(1)} + \left(\mathbf{F}\tilde{\mathbf{N}}^{\beta}\,\nu_{\beta}\right)^{(2)} = \mathbf{0} \quad \text{on } \Gamma_{\cup} \tag{39}$$

$$\left(M^{\alpha\beta}\,\mathbf{a}_{\alpha}\,\nu_{\beta}\right)^{(1)} + \left(M^{\alpha\beta}\,\mathbf{a}_{\alpha}\,\nu_{\beta}\right)^{(2)} = \mathbf{0} \quad \text{on } \Gamma_{\cup} \tag{40}$$

where the superscripts $(\cdot)^{(1),(2)}$ indicate the two domains considered herein, where $\mathbf{\Phi}$ is the rotation vector along the shell boundary which is defined as $\mathbf{\Phi} = \arcsin\left(|\mathbf{D} \times (\mathbf{d} - \mathbf{D})|\right)$. Furthermore, the deformation gradient $\mathbf{F}$ is defined as $\mathbf{F} = \mathbf{a}_{\alpha} \otimes \mathbf{A}^{\alpha} + \mathbf{d} \otimes \mathbf{D}$ and we assume the change of the element area to be small during deformation. The terms $\mathbf{F}\tilde{\mathbf{N}}^{\beta}\,\nu_{\beta}$ and $M^{\alpha\beta}\,\mathbf{a}_{\alpha}\,\nu_{\beta}$, respectively, are the boundary force and moment vectors, defined in the reference configuration where $\nu_{\beta} = \boldsymbol{\nu} \cdot \mathbf{A}_{\beta}$ is the covariant component of the unit outward normal vector $\boldsymbol{\nu}$. The vector $\tilde{\mathbf{N}}^{\beta}$ in (39) is defined as:

$$\tilde{\mathbf{N}}^{\beta} = \tilde{Q}^{\alpha\beta}\,\mathbf{A}_{\alpha} + \tilde{Q}^{\beta}\,\mathbf{D} \tag{41}$$

where the in-plane and out-of-plane force components $\tilde{Q}^{\alpha\beta}$ and $\tilde{Q}^{\beta}$, respectively, are defined as:

$$\tilde{Q}^{\alpha\beta} = \tilde{N}^{\alpha\beta} - b^{\alpha}_{\lambda}\,M^{\lambda\beta} \tag{42}$$

$$\tilde{Q}^{\beta} = M^{\alpha\beta}|_{\alpha} + a^{\beta\gamma}\left(2\,\tilde{\varepsilon}_{\gamma\lambda}|_{\mu} - \tilde{\varepsilon}_{\lambda\mu}|_{\gamma}\right)\,M^{\lambda\mu} \tag{43}$$

with $b^{\alpha}_{\lambda} = a^{\alpha\beta}\,b_{\lambda\beta} = \left(\mathbf{a}^{\alpha} \cdot \mathbf{a}^{\beta}\right)\left(\mathbf{a}_{\lambda,\beta} \cdot \mathbf{d}\right)$ being the tensor of the mixed components of the surface's second fundamental form.
The covariant derivatives of the tensor fields $M^{\alpha\beta}$ and $\tilde{\varepsilon}_{\lambda\mu}$ in (43) can be written as

$$M^{\alpha\beta}|_{\gamma} = M^{\alpha\beta}_{,\gamma} + \Gamma^{\alpha}_{\lambda\gamma}\,M^{\lambda\beta} + \Gamma^{\beta}_{\lambda\gamma}\,M^{\alpha\lambda} \tag{44}$$

$$\tilde{\varepsilon}_{\lambda\mu}|_{\gamma} = \tilde{\varepsilon}_{\lambda\mu,\gamma} - \Gamma^{\alpha}_{\lambda\gamma}\,\tilde{\varepsilon}_{\alpha\mu} - \Gamma^{\alpha}_{\mu\gamma}\,\tilde{\varepsilon}_{\lambda\alpha} \tag{45}$$

where $\Gamma^{\alpha}_{\lambda\gamma}$ is the Christoffel symbol on a surface in the reference configuration [52, 67, 68], expressed as :

$$\Gamma^{\alpha}_{\lambda\gamma} = A^{\beta\alpha}\,\Gamma_{\lambda\gamma\beta} = A^{\beta\alpha}\left(\frac{1}{2}(A_{\gamma\beta,\lambda} + A_{\lambda\beta,\gamma} - A_{\lambda\gamma,\beta})\right) \tag{46}$$

Considering the weak enforcement strategy of constraints, the variational form (26) changes to:

$$\delta\mathcal{W}_I(\delta\mathbf{u}, \delta\tilde{\boldsymbol{\varepsilon}}) + \delta\mathcal{W}_I^N(\delta\mathbf{u}, \delta\tilde{\boldsymbol{\varepsilon}}) + \delta\mathcal{W}_E(\delta\mathbf{u}) = 0 \tag{47}$$

where $\delta\mathcal{W}_I^N(\delta\mathbf{u}, \delta\tilde{\boldsymbol{\varepsilon}})$ represents the inner work contribution of the coupling conditions including consistency terms $\delta\mathcal{W}_I^{N,c}(\delta\mathbf{u}, \delta\tilde{\boldsymbol{\varepsilon}})$ and stabilization terms $\delta\mathcal{W}_I^{N,s}(\delta\mathbf{u})$. For compactness, we will write $\delta\mathcal{W}_I^{N,c}$ and $\delta\mathcal{W}_I^{N,s}$ instead of $\delta\mathcal{W}_I^{N,c}(\delta\mathbf{u}, \delta\tilde{\boldsymbol{\varepsilon}})$ and $\delta\mathcal{W}_I^{N,s}(\delta\mathbf{u})$ in the following descriptions.

The consistency terms ensure the weak enforcement of the coupling constraints between the shell patches:

$$\begin{aligned}\delta\mathcal{W}_I^{N,c} &= -\int_{\Gamma_\cup} \delta\{\mathbf{F}\tilde{\mathbf{N}}^\beta\,\nu_\beta\}\cdot[\![\mathbf{u}]\!]\,\mathrm{d}\Gamma_\cup - \int_{\Gamma_\cup}\{\mathbf{F}\tilde{\mathbf{N}}^\beta\,\nu_\beta\}\cdot\delta[\![\mathbf{u}]\!]\,\mathrm{d}\Gamma_\cup \\ &\quad -\int_{\Gamma_\cup} \delta\{M^{\alpha\beta}\,\mathbf{a}_\alpha\,\nu_\beta\}\cdot[\![\mathbf{\Phi}]\!]\,\mathrm{d}\Gamma_\cup - \int_{\Gamma_\cup}\{M^{\alpha\beta}\,\mathbf{a}_\alpha\,\nu_\beta\}\cdot\delta[\![\mathbf{\Phi}]\!]\,\mathrm{d}\Gamma_\cup \end{aligned} \tag{48}$$

where the brackets $\{\cdot\}$ and $[\![\cdot]\!]$ are the average and jump operators. The different terms are defined as follows:

$$\{\mathbf{F}\tilde{\mathbf{N}}^\beta\,\nu_\beta\} := \frac{1}{2}\left(\mathbf{F}\tilde{\mathbf{N}}^\beta\,\nu_\beta\right)^{(1)} + \frac{1}{2}\left(\mathbf{F}\tilde{\mathbf{N}}^\beta\,\nu_\beta\right)^{(2)} \tag{49}$$

$$\{M^{\alpha\beta}\,\mathbf{a}_\alpha\,\nu_\beta\} := \frac{1}{2}\left(M^{\alpha\beta}\,\mathbf{a}_\alpha\,\nu_\beta\right)^{(1)} + \frac{1}{2}\left(M^{\alpha\beta}\,\mathbf{a}_\alpha\,\nu_\beta\right)^{(2)} \tag{50}$$

$$[\![\mathbf{u}]\!] := \mathbf{u}^{(1)} - \mathbf{u}^{(2)} \tag{51}$$

$$[\![\mathbf{\Phi}]\!] := \mathbf{\Phi}^{(1)} - \mathbf{\Phi}^{(2)} \tag{52}$$

The following stabilization terms are introduced to maintain the coercivity of the bilinear form (26):

$$\delta\mathcal{W}_I^{N,s} = \int_{\Gamma_\cup} \alpha_u\,\delta[\![\mathbf{u}]\!]\cdot[\![\mathbf{u}]\!]\,\mathrm{d}\Gamma_\cup + \int_{\Gamma_\cup}\alpha_\theta\,\delta[\![\mathbf{\Phi}]\!]\cdot[\![\mathbf{\Phi}]\!]\,\mathrm{d}\Gamma_\cup \tag{53}$$

where α_u and α_θ are stabilization parameters. Optimal values of α_u and α_θ can be estimated from an element-wise local eigenvalue analysis [35, 36, 47, 69] as described in sub-section 3.4.

3.2. Discretization and linearization

The discretization of (48) and (53) provides the corresponding contributions of the Nitsche extension to the equilibrium (30):

$$\begin{aligned}\mathbf{f}_I^{N,c} &= -\int_{\Gamma_\cup} \frac{\partial\{\mathbf{F}\tilde{\mathbf{N}}^\beta\,\nu_\beta\}}{\partial(\mathbf{U},\tilde{\boldsymbol{\epsilon}})}\cdot[\![\mathbf{u}]\!]\,\mathrm{d}\Gamma_\cup - \int_{\Gamma_\cup}\{\mathbf{F}\tilde{\mathbf{N}}^\beta\,\nu_\beta\}\cdot\frac{\partial[\![\mathbf{u}]\!]}{\partial\mathbf{U}}\,\mathrm{d}\Gamma_\cup \\ &\quad -\int_{\Gamma_\cup} \frac{\partial\{M^{\alpha\beta}\,\mathbf{a}_\alpha\,\nu_\beta\}}{\partial\mathbf{U}}\cdot[\![\mathbf{\Phi}]\!]\,\mathrm{d}\Gamma_\cup - \int_{\Gamma_\cup}\{M^{\alpha\beta}\,\mathbf{a}_\alpha\,\nu_\beta\}\cdot\frac{\partial[\![\mathbf{\Phi}]\!]}{\partial\mathbf{U}}\,\mathrm{d}\Gamma_\cup \end{aligned} \tag{54}$$

$$\mathbf{f}_I^{N,s} = \int_{\Gamma_\cup}\alpha_u\,\frac{\partial[\![\mathbf{u}]\!]}{\partial\mathbf{U}}\cdot[\![\mathbf{u}]\!]\,\mathrm{d}\Gamma_\cup + \int_{\Gamma_\cup}\alpha_\theta\,\frac{\partial[\![\mathbf{\Phi}]\!]}{\partial\mathbf{U}}\cdot[\![\mathbf{\Phi}]\!]\,\mathrm{d}\Gamma_\cup. \tag{55}$$

where the derivative $\partial\{\mathbf{F}\tilde{\mathbf{N}}^\beta\,\nu_\beta\}/\partial(\mathbf{U},\tilde{\boldsymbol{\epsilon}})$ in (54) denotes

$$\frac{\partial\{\mathbf{F}\tilde{\mathbf{N}}^\beta\,\nu_\beta\}}{\partial(\mathbf{U},\tilde{\boldsymbol{\epsilon}})} = \frac{\partial\{\mathbf{F}\tilde{\mathbf{N}}^\beta\,\nu_\beta\}}{\partial\mathbf{U}} + \frac{\partial\{\mathbf{F}\tilde{\mathbf{N}}^\beta\,\nu_\beta\}}{\partial\tilde{\boldsymbol{\epsilon}}}\,. \tag{56}$$

The contributions of $\delta\mathcal{W}_I^N$ to the tangent stiffness matrix $\mathbf{K}_T$ are obtained by linearization of equations (54) and (55) in the reference configuration:

$$\begin{aligned}
\mathbf{K}_T^{N,c} &= -\int_{\Gamma_\cup} \frac{\partial\{\mathbf{F}\tilde{\mathbf{N}}^\beta\,\nu_\beta\}}{\partial(\mathbf{U},\tilde{\boldsymbol{\epsilon}})}\cdot\frac{\partial[\![\mathbf{u}]\!]}{\partial\mathbf{U}}\,\mathrm{d}\Gamma_\cup - \left[\int_{\Gamma_\cup} \frac{\partial\{\mathbf{F}\tilde{\mathbf{N}}^\beta\,\nu_\beta\}}{\partial(\mathbf{U},\tilde{\boldsymbol{\epsilon}})}\cdot\frac{\partial[\![\mathbf{u}]\!]}{\partial\mathbf{U}}\,\mathrm{d}\Gamma_\cup\right]^{\mathrm{T}} \\
&\quad -\int_{\Gamma_\cup} \frac{\partial^2\{\mathbf{F}\tilde{\mathbf{N}}^\beta\,\nu_\beta\}}{\partial(\mathbf{U},\tilde{\boldsymbol{\epsilon}})\,\partial(\mathbf{U},\tilde{\boldsymbol{\epsilon}})}\cdot[\![\mathbf{u}]\!]\,\mathrm{d}\Gamma_\cup \\
&\quad -\int_{\Gamma_\cup} \frac{\partial\{M^{\alpha\beta}\,\mathbf{a}_\alpha\,\nu_\beta\}}{\partial\mathbf{U}}\cdot\frac{\partial[\![\boldsymbol{\Phi}]\!]}{\partial\mathbf{U}}\,\mathrm{d}\Gamma_\cup - \left[\int_{\Gamma_\cup} \frac{\partial\{M^{\alpha\beta}\,\mathbf{a}_\alpha\,\nu_\beta\}}{\partial\mathbf{U}}\cdot\frac{\partial[\![\boldsymbol{\Phi}]\!]}{\partial\mathbf{U}}\,\mathrm{d}\Gamma_\cup\right]^{\mathrm{T}} \\
&\quad -\int_{\Gamma_\cup} \{M^{\alpha\beta}\,\mathbf{a}_\alpha\,\nu_\beta\}\cdot\frac{\partial^2[\![\boldsymbol{\Phi}]\!]}{\partial\mathbf{U}\,\partial\mathbf{U}}\,\mathrm{d}\Gamma_\cup - \int_{\Gamma_\cup} \frac{\partial^2\{M^{\alpha\beta}\,\mathbf{a}_\alpha\,\nu_\beta\}}{\partial\mathbf{U}\,\partial\mathbf{U}}\cdot[\![\boldsymbol{\Phi}]\!]\,\mathrm{d}\Gamma_\cup \qquad (57)
\end{aligned}$$

$$\mathbf{K}_T^{N,s} = \int_{\Gamma_\cup} \alpha_u\,\frac{\partial[\![\mathbf{u}]\!]}{\partial\mathbf{U}}\cdot\frac{\partial[\![\mathbf{u}]\!]}{\partial\mathbf{U}}\,\mathrm{d}\Gamma_\cup + \int_{\Gamma_\cup}\alpha_\theta\,\left(\frac{\partial[\![\boldsymbol{\Phi}]\!]}{\partial\mathbf{U}}\cdot\frac{\partial[\![\boldsymbol{\Phi}]\!]}{\partial\mathbf{U}} + \frac{\partial^2[\![\boldsymbol{\Phi}]\!]}{\partial\mathbf{U}\,\partial\mathbf{U}}\cdot[\![\boldsymbol{\Phi}]\!]\right)\mathrm{d}\Gamma_\cup \qquad (58)$$

where

$$\frac{\partial^2\{\mathbf{F}\tilde{\mathbf{N}}^\beta\,\nu_\beta\}}{\partial(\mathbf{U},\tilde{\boldsymbol{\epsilon}})\,\partial(\mathbf{U},\tilde{\boldsymbol{\epsilon}})} = \frac{\partial^2\{\mathbf{F}\tilde{\mathbf{N}}^\beta\,\nu_\beta\}}{\partial\mathbf{U}\,\partial\mathbf{U}} + \frac{\partial^2\{\mathbf{F}\tilde{\mathbf{N}}^\beta\,\nu_\beta\}}{\partial\mathbf{U}\,\partial\tilde{\boldsymbol{\epsilon}}} + \frac{\partial^2\{\mathbf{F}\tilde{\mathbf{N}}^\beta\,\nu_\beta\}}{\partial\tilde{\boldsymbol{\epsilon}}\,\partial\mathbf{U}}\,. \qquad (59)$$

We note that in (57), (58) and (59), the following three terms

$$\int_{\Gamma_\cup}\{\mathbf{F}\tilde{\mathbf{N}}^\beta\,\nu_\beta\}\cdot\frac{\partial^2[\![\mathbf{u}]\!]}{\partial\mathbf{U}\,\partial\mathbf{U}}\,\mathrm{d}\Gamma_\cup \qquad (60)$$

$$\int_{\Gamma_\cup}\alpha_u\,\frac{\partial^2[\![\mathbf{u}]\!]}{\partial\mathbf{U}\,\partial\mathbf{U}}\cdot[\![\mathbf{u}]\!]\,\mathrm{d}\Gamma_\cup \qquad (61)$$

$$\frac{\partial^2\{\mathbf{F}\tilde{\mathbf{N}}^\beta\,\nu_\beta\}}{\partial\tilde{\boldsymbol{\epsilon}}\,\partial\tilde{\boldsymbol{\epsilon}}} \qquad (62)$$

have been dropped due to the interpolation relations of the displacement field in (27) and the assumed membrane strain field in (29).

Taking the derivatives of the force vector $\{\mathbf{F}\tilde{\mathbf{N}}^\beta\,\nu_\beta\}$, bending moment $\{M^{\alpha\beta}\,\mathbf{a}_\alpha\,\nu_\beta\}$ and rotations $[\![\boldsymbol{\Phi}]\!]$ with respect to the displacement and assumed membrane strain variables results in a number of terms, which demand a careful computer implementation. We present the detailed derivation of the force vector derivatives in Appendix A, while for the derivatives of bending moments and rotations, we refer the reader to our previous work in [22].

It is worth to note that in a linear theory, the contributions of $\delta\mathcal{W}_I^N$ to the tangent stiffness matrix $\mathbf{K}_T$ can be simplified by evaluating (57) and (58) in the reference configuration as:

$$\mathbf{K}_{T,L}^{N,c} = \left(-\int_{\Gamma_\cup} \frac{\partial\{\mathbf{F}\tilde{\mathbf{N}}^\beta\,\nu_\beta\}}{\partial(\mathbf{U},\tilde{\boldsymbol{\epsilon}})}\cdot\frac{\partial[\![\mathbf{u}]\!]}{\partial\mathbf{U}}\,\mathrm{d}\Gamma_\cup - \left[\int_{\Gamma_\cup} \frac{\partial\{\mathbf{F}\tilde{\mathbf{N}}^\beta\,\nu_\beta\}}{\partial(\mathbf{U},\tilde{\boldsymbol{\epsilon}})}\cdot\frac{\partial[\![\mathbf{u}]\!]}{\partial\mathbf{U}}\,\mathrm{d}\Gamma_\cup\right]^{\mathrm{T}}\right.$$

$$- \int_{\Gamma_\cup} \frac{\partial \{M^{\alpha\beta}\, \mathbf{a}_\alpha\, \nu_\beta\}}{\partial \mathbf{U}} \cdot \frac{\partial [\![\mathbf{\Phi}]\!]}{\partial \mathbf{U}}\, \mathrm{d}\Gamma_\cup - \left[\int_{\Gamma_\cup} \frac{\partial \{M^{\alpha\beta}\, \mathbf{a}_\alpha\, \nu_\beta\}}{\partial \mathbf{U}} \cdot \frac{\partial [\![\mathbf{\Phi}]\!]}{\partial \mathbf{U}}\, \mathrm{d}\Gamma_\cup \right]^{\mathrm{T}} \Bigg) \Bigg|_{\substack{\tilde{\boldsymbol{\epsilon}}=0 \\ \mathbf{U}=0}} \tag{63}$$

$$\mathbf{K}^{N,s}_{T,L} = \left(\int_{\Gamma_\cup} \alpha_u\, \frac{\partial [\![\mathbf{u}]\!]}{\partial \mathbf{U}} \cdot \frac{\partial [\![\mathbf{u}]\!]}{\partial \mathbf{U}}\, \mathrm{d}\Gamma_\cup + \int_{\Gamma_\cup} \alpha_\theta\, \frac{\partial [\![\mathbf{\Phi}]\!]}{\partial \mathbf{U}} \cdot \frac{\partial [\![\mathbf{\Phi}]\!]}{\partial \mathbf{U}}\, \mathrm{d}\Gamma_\cup \right) \Bigg|_{\mathbf{U}=0} \tag{64}$$

3.3. Integration of the Nitsche coupling terms along trimming curve

For the weak coupling between trimmed shell patches, the integration of the variational coupling terms (54), (55), (57) and (58) are performed segment-wise along the physical curve (see Figure 6). We first compute the intersection points of the parametric curves in each surface patch with all knot lines of Bézier elements. These intersection points are then mapped to the physical curve with their corresponding parametric coordinates on the physical curve, computed simultaneously. Combining the new parametric coordinates and the original knot values of the physical curve, they form the integration knot spans. We then place Gaussian quadrature points within each knot span of the physical curve and map them back to the two parametric spaces of the two patches. Through this procedure, the contributions of the Nitsche terms are evaluated accurately.

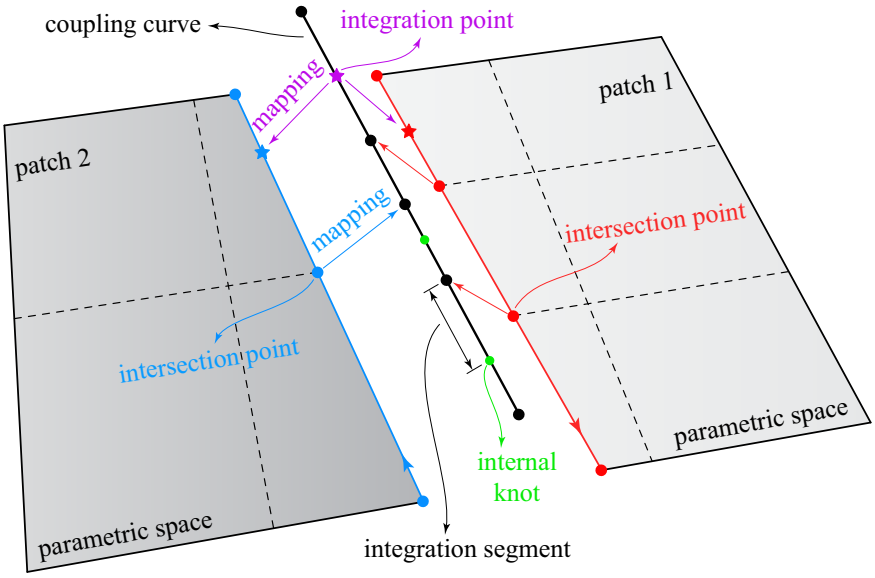

Figure 6: Schematic representation of the segment-wise integration of the coupling terms.

3.4. Element-wise estimation of stabilization parameters

The use of stabilization terms, cf eq. (53), ensures coercivity of the formulation. For trimmed shell problems, the stabilization parameters α_u and α_θ should be tailored for each pair of coupled elements such that the element with the worst cut does not deteriorate the accuracy of the total solution. We follow an approach reported in [35, 47] to estimate element-wise optimal parameters based on a local eigenvalue problem. Using a general inverse estimate, it can be shown that the stabilization parameters α_u and α_θ depend on mesh-dependent positive constants C_u and C_θ,

respectively, defining upper bounds for the flux along the coupling interface in terms of the strain energy of the coupled domains [70, 71]:

$$\| \{\mathbf{F}\tilde{\mathbf{N}}^{\beta}\, \nu_{\beta}\} \|^2_{\Gamma_\cup} \;\leq\; C_u\, (\mathcal{W}_I^{(1)} + \mathcal{W}_I^{(2)}) \tag{65}$$

$$\| \{M^{\alpha\beta}\, \mathbf{a}_{\alpha}\, \nu_{\beta}\} \|^2_{\Gamma_\cup} \;\leq\; C_\theta\, (\mathcal{W}_I^{(1)} + \mathcal{W}_I^{(2)}) \tag{66}$$

with $\| \cdot \|$ being the L^2-norm of the quantity.

Making use of Young's inequality, we can obtain a lower bound of the inner work enriched with Nitsche terms, and the coercivity of the formulation can be ensured when the stabilization parameters $\alpha_u > 2\, C_u$ and $\alpha_\theta > 2\, C_\theta$ [36, 47]. In [70] it is shown that optimal values for the two constants C_u and C_θ are maximizers of the Rayleigh quotient of the inverse estimates (65) and (66), respectively, and hence can be found as the largest eigenvalues of the generalized eigenvalue problem:

$$\mathbf{A}\mathbf{u} \;=\; \lambda\, \mathbf{B}\mathbf{u} \tag{67}$$

where matrix $\mathbf{B}$ is defined as the sum of the element stiffness matrices involved in the coupling:

$$\mathbf{B} \;=\; \sum_{e=1}^{2} (\mathbf{K}_T)_e \tag{68}$$

with $\mathbf{K}_T$ according to (35) and (36).
For the estimation of C_u and C_θ, the matrix $\mathbf{A}$ is defined, respectively, as:

$$\mathbf{A}^u \;=\; 2 \int_{\Gamma_\cup} \left(\frac{\partial \{\mathbf{F}\tilde{\mathbf{N}}^{\beta}\, \nu_{\beta}\}}{\partial (\mathbf{U}, \tilde{\boldsymbol{\epsilon}})} \cdot \frac{\partial \{\mathbf{F}\tilde{\mathbf{N}}^{\beta}\, \nu_{\beta}\}}{\partial (\mathbf{U}, \tilde{\boldsymbol{\epsilon}})} + \frac{\partial^2 \{\mathbf{F}\tilde{\mathbf{N}}^{\beta}\, \nu_{\beta}\}}{\partial (\mathbf{U}, \tilde{\boldsymbol{\epsilon}})\, \partial (\mathbf{U}, \tilde{\boldsymbol{\epsilon}})} \cdot \{\mathbf{F}\tilde{\mathbf{N}}^{\beta}\, \nu_{\beta}\} \right) d\Gamma_\cup \tag{69}$$

$$\mathbf{A}^\theta \;=\; 2 \int_{\Gamma_\cup} \left(\frac{\partial \{M^{\alpha\beta}\, \mathbf{a}_{\alpha}\, \nu_{\beta}\}}{\partial \mathbf{U}} \cdot \frac{\partial \{M^{\alpha\beta}\, \mathbf{a}_{\alpha}\, \nu_{\beta}\}}{\partial \mathbf{U}} + \frac{\partial^2 \{M^{\alpha\beta}\, \mathbf{a}_{\alpha}\, \nu_{\beta}\}}{\partial \mathbf{U}\, \partial \mathbf{U}} \cdot \{M^{\alpha\beta}\, \mathbf{a}_{\alpha}\, \nu_{\beta}\} \right) d\Gamma_\cup \tag{70}$$

where the derivatives of $\{\mathbf{F}\tilde{\mathbf{N}}^{\beta}\, \nu_{\beta}\}$ are described in Appendix A and the derivatives of $\{M^{\alpha\beta}\, \mathbf{a}_{\alpha}\, \nu_{\beta}\}$ can be found in [22]. Again, the matrices $\mathbf{A}^u$, $\mathbf{A}^\theta$ and $\mathbf{B}$ can be further simplified for linear elastic shell problems, cf [34].

4. Numerical Examples

In this section, we test the proposed method with a number of numerical examples to reveal the reliability, accuracy and robustness. In particular, we consider aspects regarding the elimination of membrane locking and a proper transfer of the elastic response among the patches according to the specified interface conditions (37)-(40). To this end, we start with two examples of linear elasticity for a critical comparison of the result with previous test results of a pure single-field theory and to

receive a first impression on the method's performance with regard to locking, cf sub-section 4.1. We then consider the non-linear response behavior of our coupling formulation in terms of large displacements and structural stability, cf sub-section 4.2.
Notation: In this section we repeatedly compare two models according to different theories which we denote for brevity as follows: (i) a pure displacement-based Kirchhoff-Love shell model referred to as *single-field model*, (ii) a Hellinger-Reissner extendend Kirchhoff-Love shell model referred to as *mixed model*.

4.1. Multi-patch analysis – linear elasticity

The first example considers a cylindrical shell strip to study the locking behavior in presence of high aspect ratios [11]. The example is a customary benchmark considering the influence of the radius-to-thickness ratio on the shell deformation. The second example is taken from the shell obstacle course considered in [66, 72] with a particular focus on the reliability of the stress resultants for low polynomial orders which may lead to undesirable oscillations [73].

4.1.1. Cylindrical shell strip problem

The cylindrical shell strip depicted in Figure 7 is studied for different radius-to-thickness ratios e.g. $R/t = 5, 10, 10^2, 10^3$ and 10^4, to study the phenomenon of membrane locking, where t denotes the shell thickness. The geometric description, material properties and boundary conditions are shown in Figure 7(a). The shell strip is clamped at one end and subjected to a uniform line load $q_x = 0.1 \cdot t^3$ at the other end.

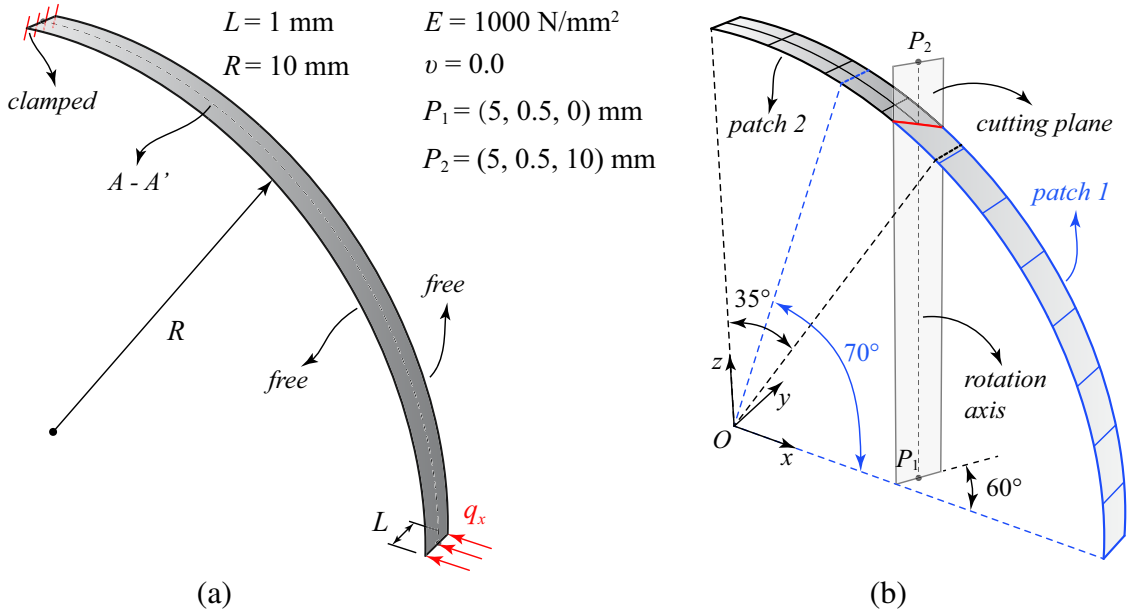

Figure 7: Cylindrical shell strip: (a) model description, (b) two-patch trimmed configuration and NURBS meshes.

We assembled the model using two overlapping circular arc shell patches with center angle $\theta_1 = 70°$ and $\theta_2 = 35°$, respectively, cf. Figure 7(b). The two patches were trimmed by a cutting

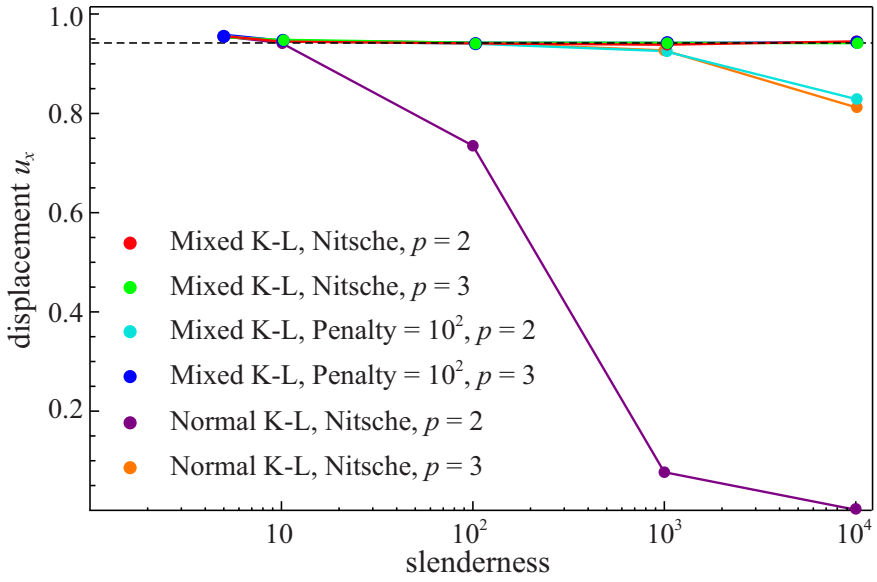

Figure 8: Cylindrical shell strip: displacements vs. slenderness.

plane and coupled at the common trimming edge. The cutting plane is defined by a vertical rotational axis, with end points P_1 and P_2, and a rotation angle of $60°$ in the $x - y$ plane. The shell patches were discretized by 9×1 and 4×2 NURBS elements for patch 1 and patch 2, respectively. A polynomial order of $p = q = 2$ and $p = q = 3$ were chosen for the analysis.

In Figure 8, the radial displacement of the free loading edge of the shell w.r.t. the slenderness R/t is shown. A radial reference displacement of 0.942 which is independent of the slenderness was derived according to the Euler-Bernoulli theory in [11]. We compare three different models: (i) the mixed model using Nitsche-type coupling, (ii) the mixed model using a pure penalty-based coupling, and (iii) a single-field model with Nitsche-type coupling.
A severe membrane locking was observed for the single field solution (iii) with $p = q = 2$, even for a moderate slenderness of $R/t = 100$. With increasing slenderness the displacements decreased rapidly to an almost complete displacement locking at $R/t = 10^4$. Order elevation to $p = q = 3$ alleviated the locking phenomenon for low aspect ratios but again emerged for increasing slenderness. In contrast, the mixed models (i) and (ii) revealed their potential to remove locking by the independent strain interpolation. In combination with the stabilized Nitsche-type coupling, model (i), we observed a stable and accurate agreement with the reference solution irrespective of any slenderness degrees. The penalty coupling behaves significantly weaker. Model (ii) showed a strong dependency on the empirically chosen penalty parameter. Therefore, we analyzed the impact of the penalty parameter on membrane locking, depicted in Figure 9. Three different penalty factors were considered: 10^2, 10^3 and 10^6. Surprisingly, larger penalty values deteriorated the performance of the mixed shell element for higher slenderness values. This behavior contradicts the basic principles of the penalty method and underlines its variational inconsistency.

We further studied the quality of the bending moments across the coupling interface of the

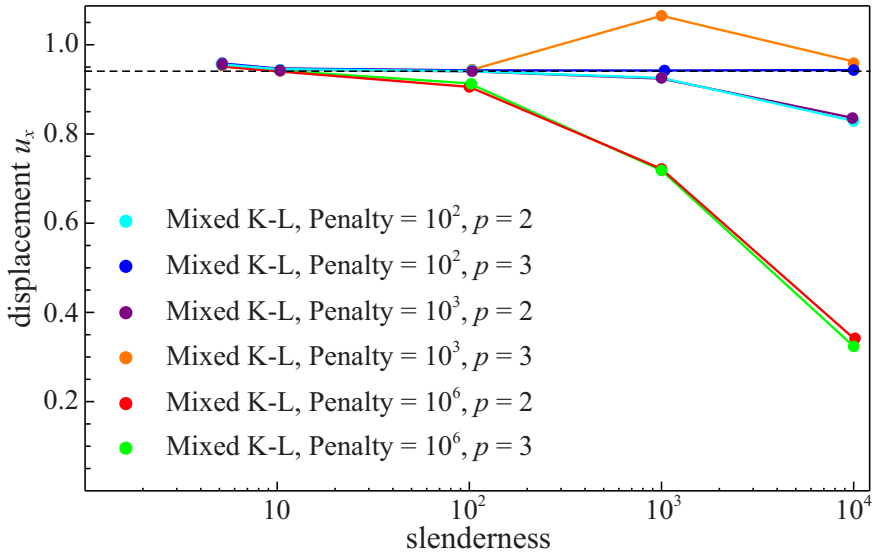

Figure 9: Cylindrical shell strip: impact of the penalty parameter.

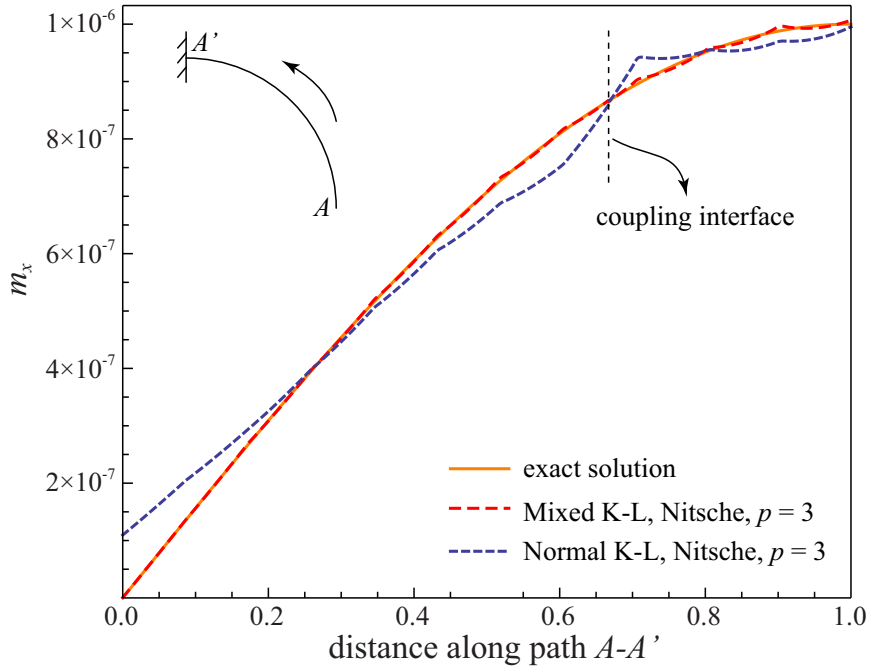

Figure 10: Cylindrical shell strip with slenderness R/t = 10^3: comparisons of bending moments.

shell model, which involves the second order derivatives of the displacement field. In Figure 10, the bending moment m_x is plotted along the path $A - A'$ for both, the mixed and single-field model, with a slenderness of $R/t = 10^3$. An exact solution can be derived from the equilibrium of the shell strip which is also shown in Figure 10. The mixed model is in excellent agreement with the exact solution without any noteworthy jumps along the coupling interface. In contrast, the

single-field model shows evident deviations from the exact solution which confirms the existence of membrane locking.

4.1.2. Scordelis-Lo roof

In this example, we consider the Scordelis-Lo roof subjected to a self-weight loading. The geometric description and the material properties are shown in Figure 11(a). The roof structure has rigid diaphragms at the curved boundaries and is free at the straight edges. We modeled the roof with two trimmed patches with a cutting plane as defined in Figure 11(b) with $\theta = 12.25°$. The two coupled patches are identical, each representing a full geometric model of the Scordelis-Lo roof and fading out the corresponding trimmed overlap. They were discretized with 17×14 and 18×13 NURBS elements, respectively.

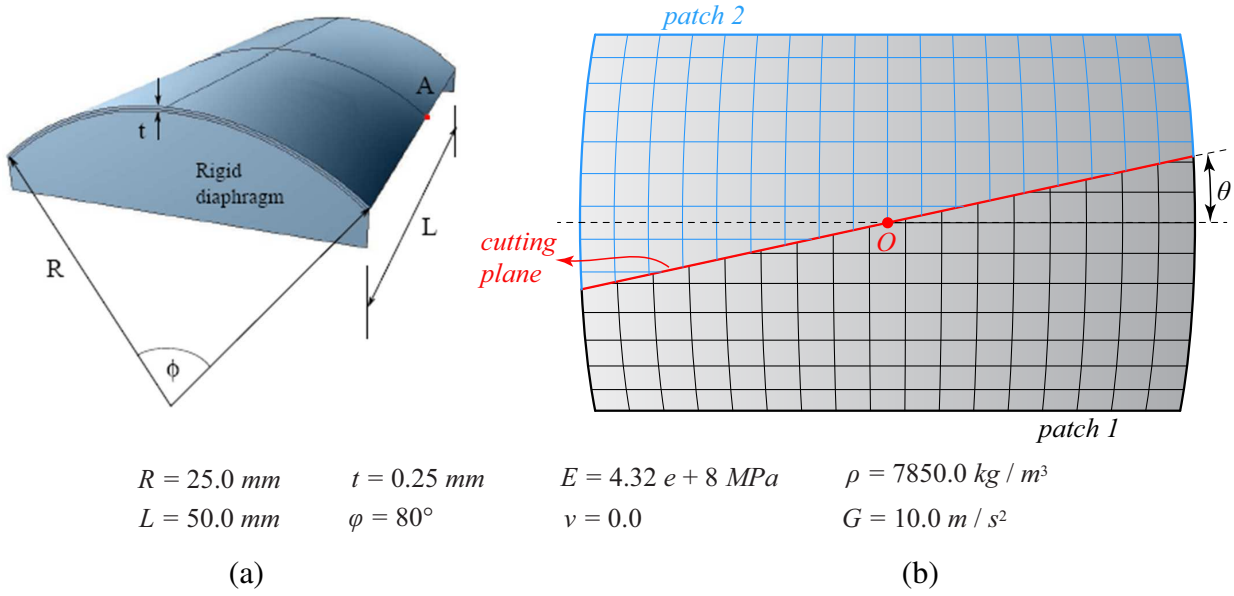

Figure 11: Scordelis-Lo's roof: (a) model description, (b) trimmed two-patch configuration and NURBS meshes.

In Figure 12, we show convergence plots of the vertical displacement at point A versus the number of control points. A reference value of $u_z = 0.3006$ mm for the vertical displacement at point A was taken from [1]. Three different models with polynomial degrees $p = q = 2$ and $p = q = 3$ were studied: (i) a mixed model with Nitsche-type coupling, (ii) a mixed model with penalty-based coupling and (iii) a single-field model with Nitsche-type coupling. The results shown in Figure 12 confirm the previous observations made for the cylindrical shell strip example. The mixed formulation converged faster compared to the single-field shell model. Again, the quadratic NURBS basis behaved significantly weaker in terms of convergence speed compared to the cubic models. Besides, the mixed shell model with Nitsche-type coupling converged slightly faster than its penalty counterpart with a penalty factor of 10^3.

In Figure 13, we show the convergence of a h-refinement in terms of the error in energy norm versus the element sizes of the three models. The convergence plot for two different penalty values, 10^2 and 10^3, which turned out to the most stable and accurate choices among a variety of

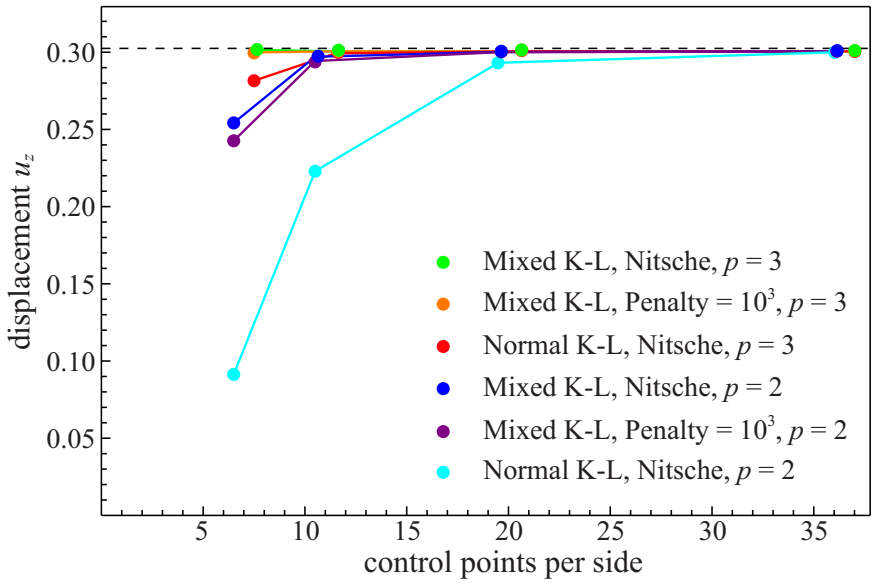

Figure 12: Scordelis-Lo's roof: convergence of the displacement.

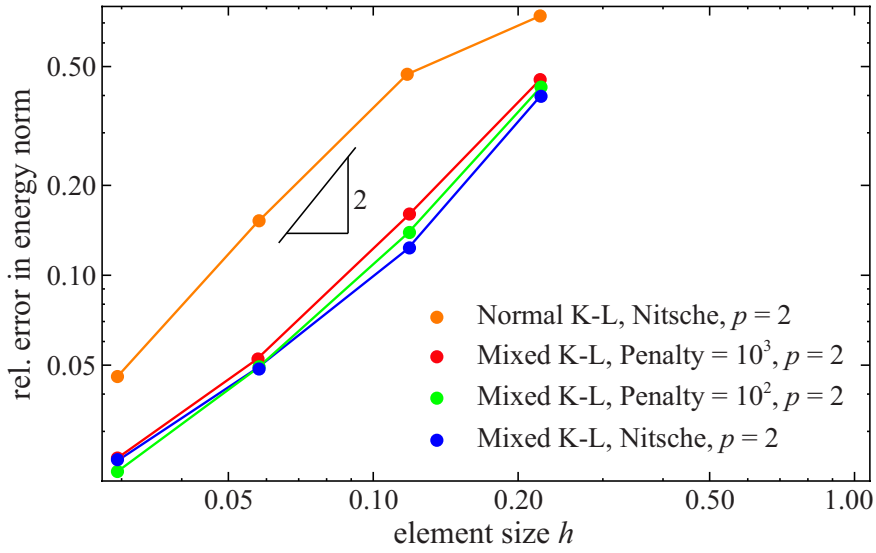

Figure 13: Scordelis-Lo roof: convergence of the strain energy.

tested values, were selected to disclose the sensitivity of the method with respect to the elastic response. A reference strain energy[1] was computed by extrapolating single-patch results of a uniform $p-$refinement [74]. Both, the mixed and the single-field shell model virtually show the same rate of convergence in energy norm. Moreover, the mixed model shows the expected impact of mixed formulations on the accuracy level of the solution but keeps the rate of convergence unaffected. Again, the shell models using the Nitsche-type coupling predict the elastic response

[1] $\Pi = 4826.577066016016$

slightly better than the penalty-based models.

An interesting aspect with regard to the presented extensions of sections 2 and 3 is the solution of the inner forces in terms of stress resultants. To this end, we investigated the quality of the dominating stress resultants n_{11} of the coupled multi-patch models applying an in-plane cubic order $p = q = 3$. Subscript $\{11\}$ denotes the curved edge direction of the roof.

In Figure 14 the contour plots of n_{11} of the mixed and single-field Kirchhoff-Love shell models are presented. The mixed Kirchhoff-Love model shows an excellent quality disclosing a smooth distribution of the stress resultant at all levels including a perfect match of the flux of the two patches along the common interface. In contrast, the single-field Kirchhoff-Love model is dominated by a strong oscillatory distribution of n_{11} in the compression zone. The drop in quality between the two models is easily quantified by the minimum and maximum values of n_{11} which show a relative difference of 5.25% for the minimum value and a more than 6 times higher value for the maximum value of the single-field solution.

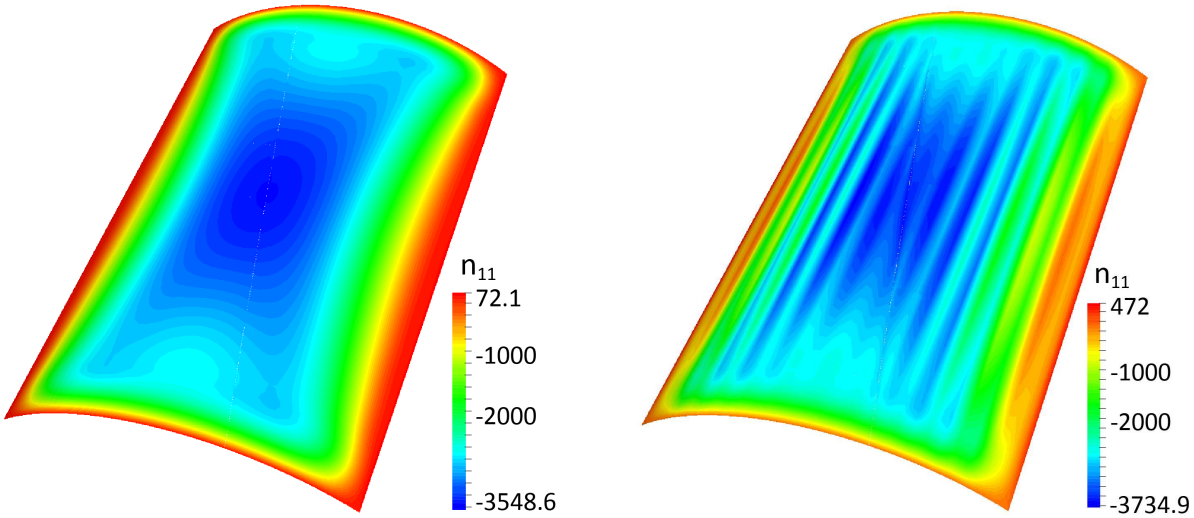

(a) (b)

Figure 14: Stress resultants n_{11} of Scordelis-Lo roof: (a) mixed Kirchhoff-Love shell with Nitsche's coupling method, (b) single-field Kirchhoff-Love shell with Nitsche's coupling method.

The stress resultant n_{11} along the coupling interface is plotted in Figure 15 along the trimmed coupling curve for the considered models. The plots confirm the quality jumps among the different models. A slight jump in the plot of the mixed model was identified at two locations where very small trimmed elements appeared, still providing an overall accurate, smooth and reliable result.

4.2. Multi-patch analysis – geometrically non-linear

In the following, we consider the performance of the proposed extension to geometrically non-linear analyses. For this purpose, we selected the deformation analysis of a slit annular plate [75] and a stability analysis of a snap-through behavior of a crossing tubes model [38]. The first example is a classical benchmark problem in the framework of geometric non-linear analyses with interesting implications with regard to a stable load step size. The second example is taken

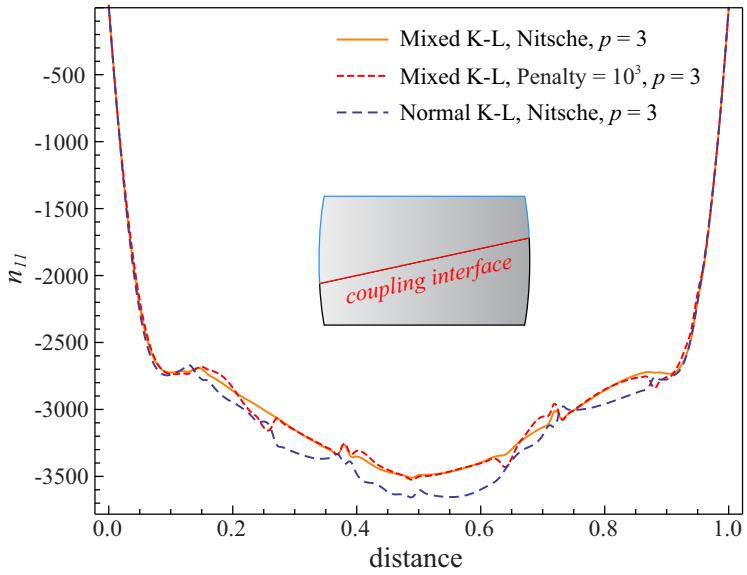

Figure 15: Scordelis-Lo roof: plots of stress resultants n_{11} along trimmed coupling curve.

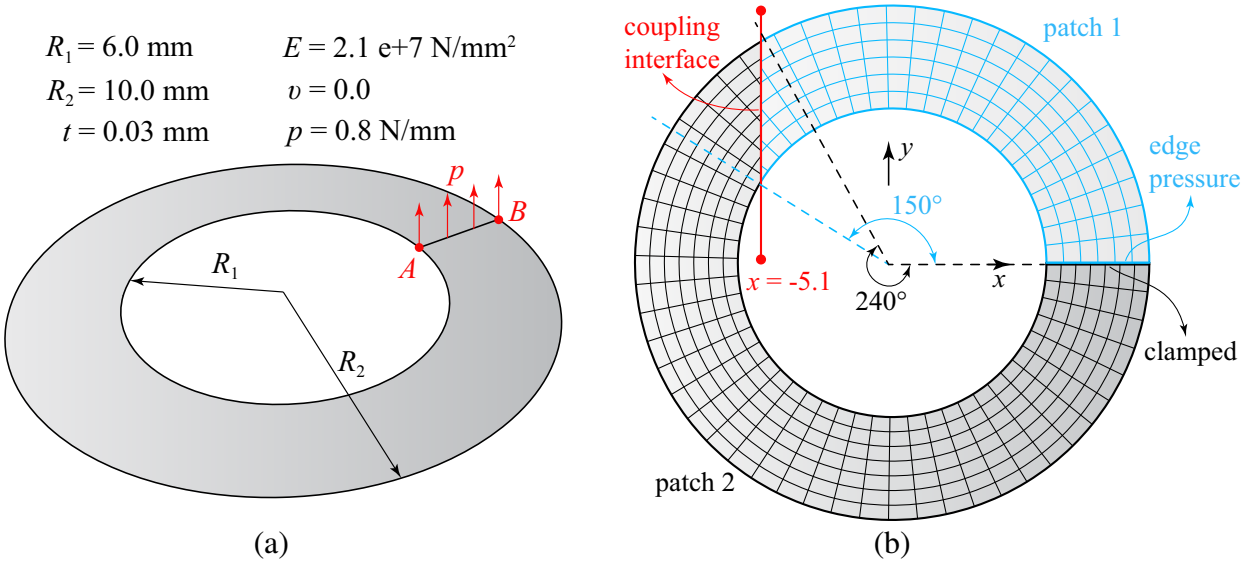

Figure 16: Slit annular plate: (a) model description, (b) two-patch trimmed configuration and NURBS meshes.

from a previously published paper [38] of the authors which represents a model with relevance in engineering.

4.2.1. Slit annular plate problem

We consider a slit annular plate under uniform line pressure loading on one end and fixed boundary conditions [76, 77] at the other end. The geometry and material properties of the plate are depicted in Figure 16(a). We assembled a multi-patch model from two trimmed patches with circular angles $150°$ and $240°$, respectively. The two patches are discretized with 23×6 and 37×7

cubic NURBS elements, and connected along a vertical trimming line at $x = -5.1mm$, cf. Figure 16(b). We used the geometrically non-linear Nitsche-type coupling for both, the mixed and the single-field model. The values of the stabilization parameters α_u and α_θ were determined from the solution of a local eigenvalue analysis at the beginning of the first load step and kept constant during the entire loading process. Comparing the element-wise computed eigenvalues of the first and last load step, we found that on average, the values changed by approximately 2% for α_θ and by approximately 0.1% for α_u, which justifies our strategy.

It is important to note that reference solutions based on a pure single-field theory, in general, either fail for larger step sizes or require an excessive number of iterations to regain control over equilibrium path. A common strategy applied in literature is to adjust the step size during the computation, starting with smaller load increments in the first steps. In Table 1, first result column (case 1), we show the maximum step size for the first load step which ensures convergence and the corresponding total number of equilibrium iterations for the mixed and single-field model. In comparison with the single-field model, the model of the mixed formulation exhibits a superior convergence behavior in various aspects: (i) the step size of the first load step of the mixed model could be chosen almost 10 times larger ($\lambda = 0.94/0.95$) than for the single-field model ($max\lambda = 0.1$), still providing a stable analysis. The single-field model failed to converge for load step sizes larger than $\lambda = 0.1$. (ii) In total, only two load steps were necessary using the mixed model to trace the entire equilibrium path, while the single-field model used 20 steps with a load step size of 0.05 to ensure a balanced number of equilibrium iterations. (iii) The total number of Newton iterations for the mixed shell model reached a minimum of 15 cycles, while the single-field model required around 140 iteration to ensure equilibrium.

Table 1: Slit annular plate: comparisons of load steps and total number of iterations.

model	max. first load step size λ_1	total No. iterations case 1	total No. iterations case 2
mixed single patch	0.95	17 + 3 (λ_1 = 0.95, λ_2 = 0.05)	8 + 7 (λ_1 = 0.75, λ_2 = 0.25)
mixed multi-patch	0.94	12 + 3 (λ_1 = 0.94, λ_2 = 0.06)	8 + 7 (λ_1 = 0.75, λ_2 = 0.25)
single-field single patch	0.05	142 (λ = 0.05, 20 load steps)	
single-field multi-patch	0.05	140 (λ = 0.05, 20 load steps)	
ABAQUS [75]	-	346 (67 load steps)	

In the second result column of Table 1, we show the influences of different loading sequences on the total number of iterations for the mixed shell models. Compared to result column 1 (case 1) where we tested the stability of the analysis for the maximum first step size, the application of a more balanced step size (case 2) resulted in a better balanced and finally decreased number of equilibrium iterations. In comparison with the established standard in shell analysis, represented

by an ABAQUS solution [75] obtained with 80×10 $S4R$ shell elements, the total number of load steps and required equilibrium iterations dropped significantly by more than one order of magnitude, cf. Table 1.

In Figure 17(a), we show a comparison of the load-displacement curves between the multi-patch mixed shell model and a reference solution taken from [75]. A two step loading process with $\lambda_1 = 0.75$ and $\lambda_2 = 0.25$ was sufficient to arrive at the final solution of the equilibrium path with excellent agreement among the two solutions. In Figure 17(b) the displacement contour plot of the multi-patch mixed shell model at the final loading step is depicted.

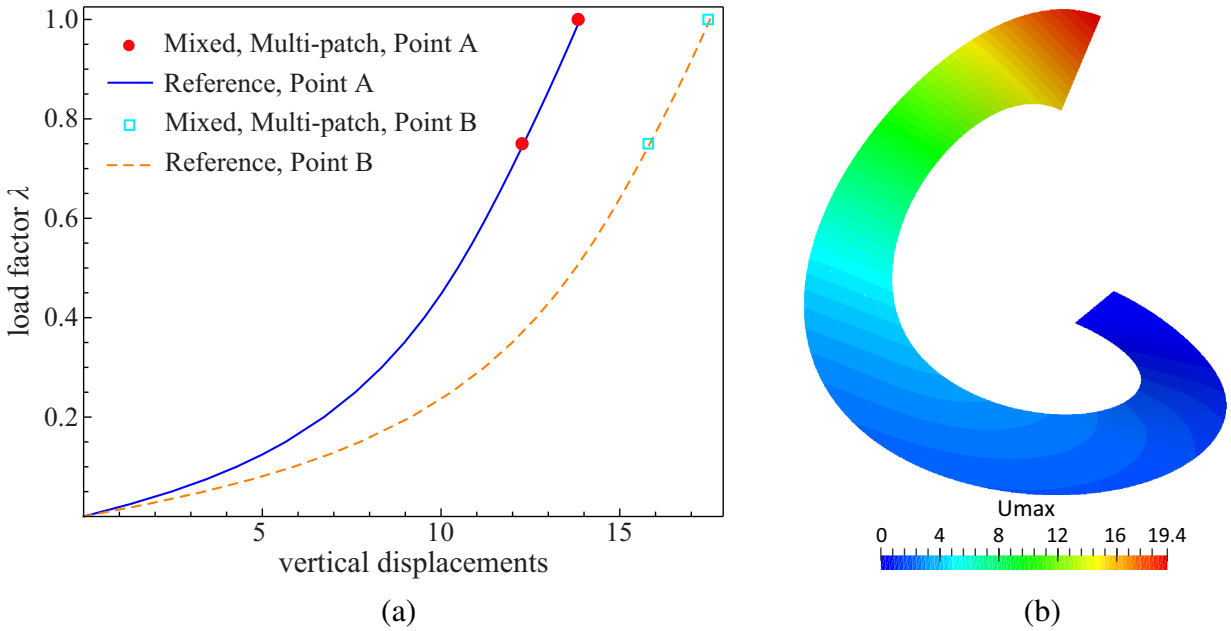

Figure 17: Slit annular plate (order of the basis $p = q = 3$): (a) comparisons of load displacements, (b) final deformed shapes of mixed multi-patch shell models.

The solution quality for the coupling interface is shown in the plots of the stress resultants and bending moments along the trimming line depicted in Figure 18. A reference solution was obtained from a single patch mixed shell model with a discretization of 59×8 cubic NURBS elements. Good agreements between the multi-patch and single patch mixed models were found for both stress resultants and bending moments. The stress resultant of the single-field model agrees quite well with the reference solutions, though the bending moment slightly oscillates around the reference solutions which indicates the inaccuracy of the second order derivatives of the displacement field. The contour plots of the stress resultant component n_y and bending moment component m_x of the multi-patch mixed model are presented in Figure 19 revealing a completely smooth and continuous transition across the trimming interface. For the sake of convenience in the illustration of the contour plots, we transformed the above quantities from the local to the global Cartesian basis.

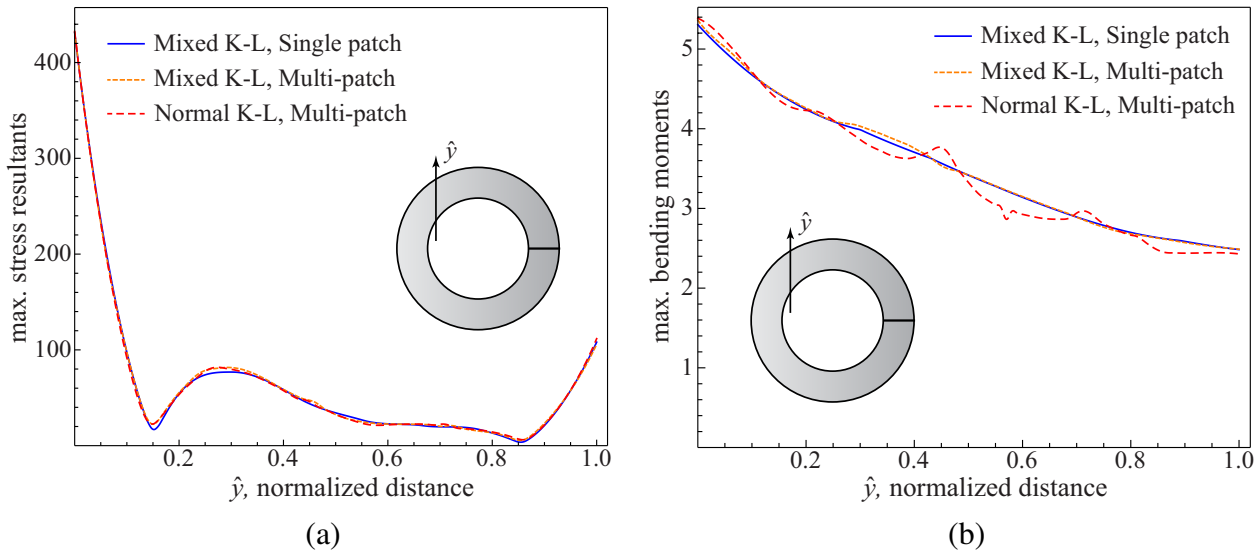

Figure 18: Slit annular plate (order of the basis $p = q = 3$): (a) comparisons of stress resultants along trimming line, (b) comparisons of bending moments along trimming line.

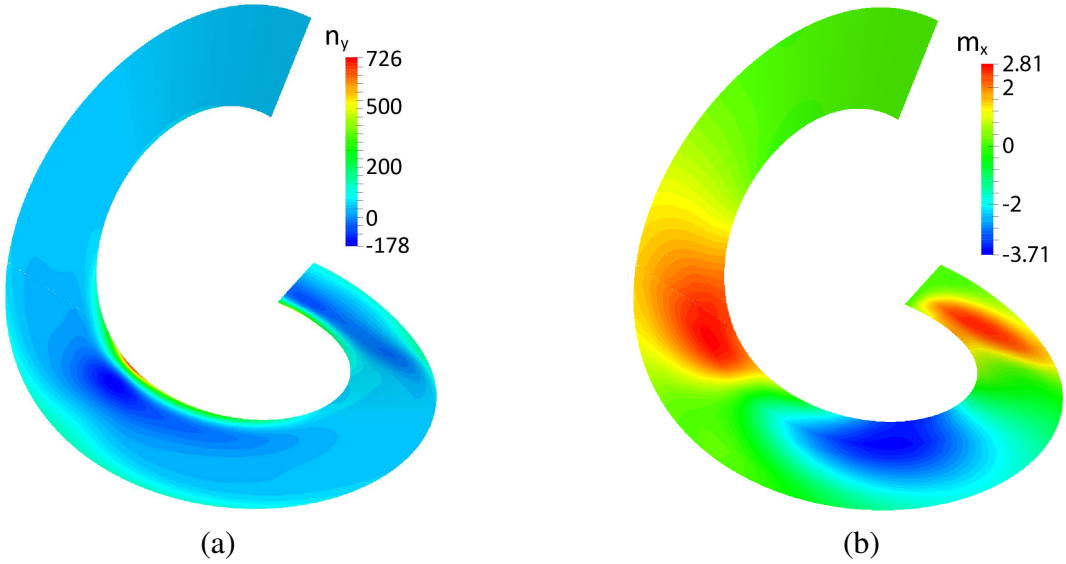

Figure 19: Contour plots of the slit annular plate modeled with multi-patch mixed Kirchhoff-Love shell elements (order of the basis $p = q = 3$): (a) stress resultants n_y, (b) bending moments m_x.

4.2.2. Snap-through of crossing tubes

Finally, we demonstrate the performance of the proposed Nitsche-type coupling with a more complex example from engineering which exhibits a snap-through buckling behavior. To this end, we have selected a CAD-derived multi-patch NURBS model which was designed with the freeform modeler Rhino3D[78]. In GUO ET AL. [22], we have demonstrated the complete work-flow for the design and derivation of an analysis suited model based on native CAD data including

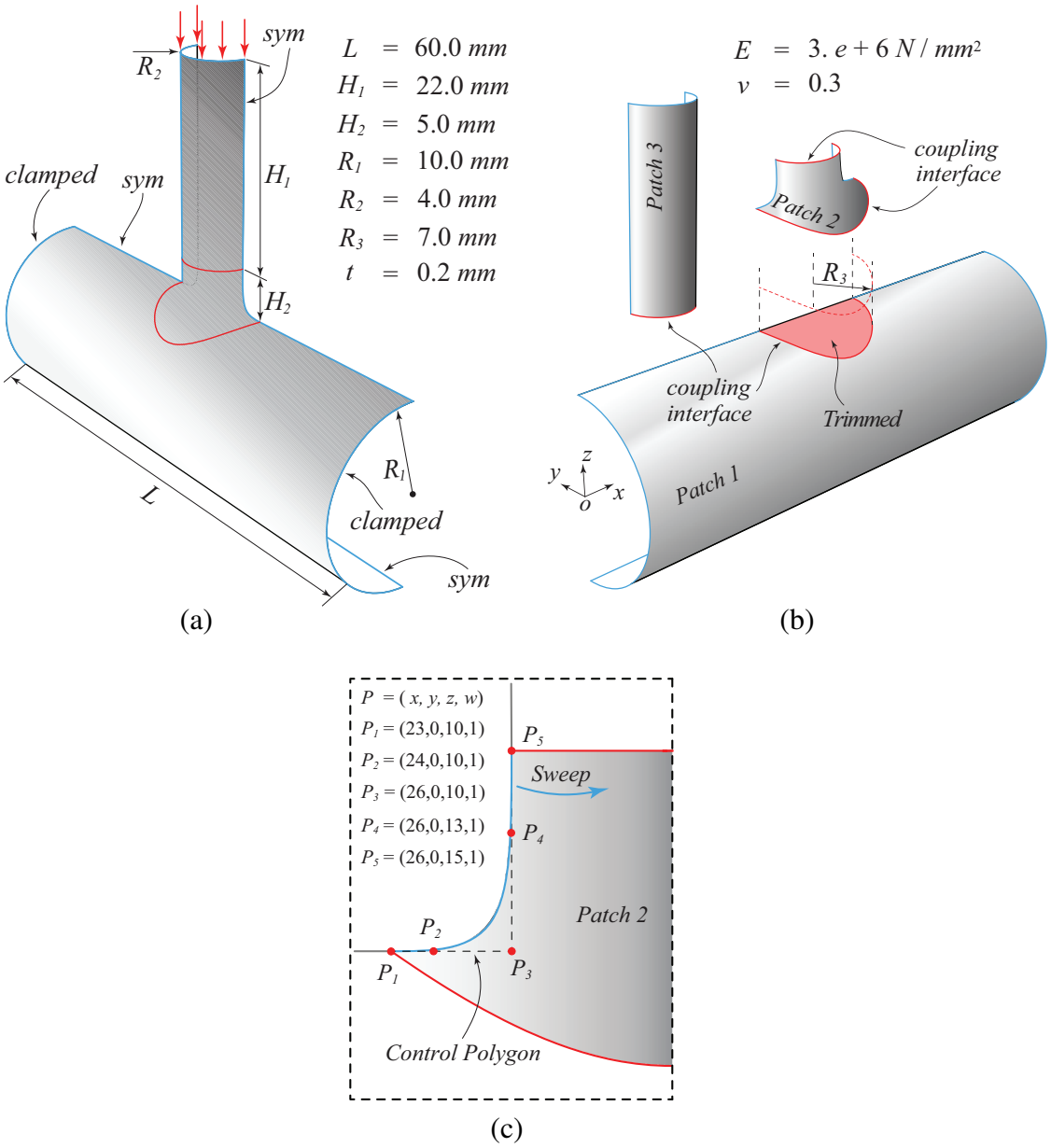

Figure 20: Multi-patch crossing tubes model: (a) geometry, boundary conditions and material properties, (b) multi-patch model, (c) detailed geometry of the connection.

trimming and coupling. Due to the structural symmetry, only one half of the model was considered, cf. Figure 20. The connection of the two perpendicular tubes was designed with a NURBS curve, swept along the interfaces, cf. Figure 20(c). Patch 1 was discretized with 62×40 elements, patch 2 with 38×28 elements and patch 3 with 24×16 elements. The polynomial degree was selected to be $p = q = 2$ and $p = q = 3$. The intersecting tube was subjected to a uniform pressure at the top of the vertical tube. The total structure was clamped at the two ends of the horizontal tube. We used an arc-length path-following method to trace the complete equilibrium path of the

snap-through phenomenon [79–81].

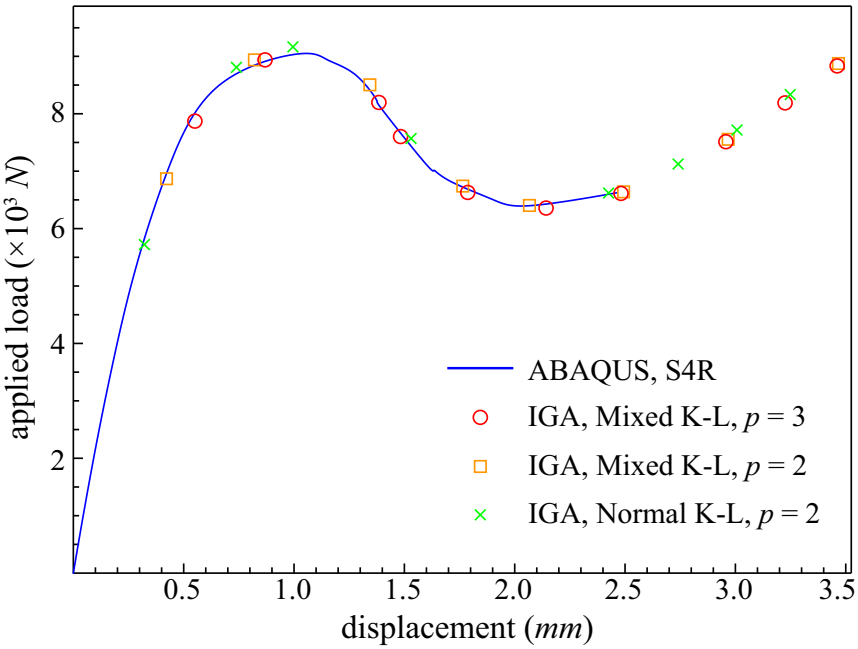

Figure 21: Multi-patch crossing tubes: comparisons of load-displacement curves.

Figure 21 depicts the load-displacement responses for both, the IGA solution and a FEM reference solution (ABAQUS) [82], obtained from a discretization with 39280 $S4R$ elements and measured at the top rim of the vertical tube. The presented displacements were chosen as the average of the control point displacements for the IGA model and the average of FE node displacements (ABAQUS) on the loading edge, respectively. An overall good agreement between the ABAQUS and IGA solution was observed. It is worth to mention that, during the post-buckling state, the ABAQUS reference solution which is based on a four node reduced integration Reissner-Mindlin shell element, failed at a maximum displacement of $u_z = 2.463\,mm$, cf. blue curve in Figure 21. In contrast, both isogeometric models easily surpassed the limit points and reached a much larger post-buckling deformations than ABAQUS solutions.

In Figure 22 we compare the contour plots of the stress resultant component n_z between the mixed and single-field model. Both models are in the pre-buckling state with an externally applied load of $8796.5N$. As observed in the first example, membrane locking leads to severe oscillations in the stress resultant n_z of the single-field model, cf. Figure 22(b), whereas the mixed model shows a smooth distribution of n_z all over, cf. Figure 22(a).

The deformed structure in the snap-through state is shown in Figure 23. It's worth to note that the inherent continuity and smoothness properties of NURBS patches were fully preserved along the non-conforming and trimmed coupling interfaces.

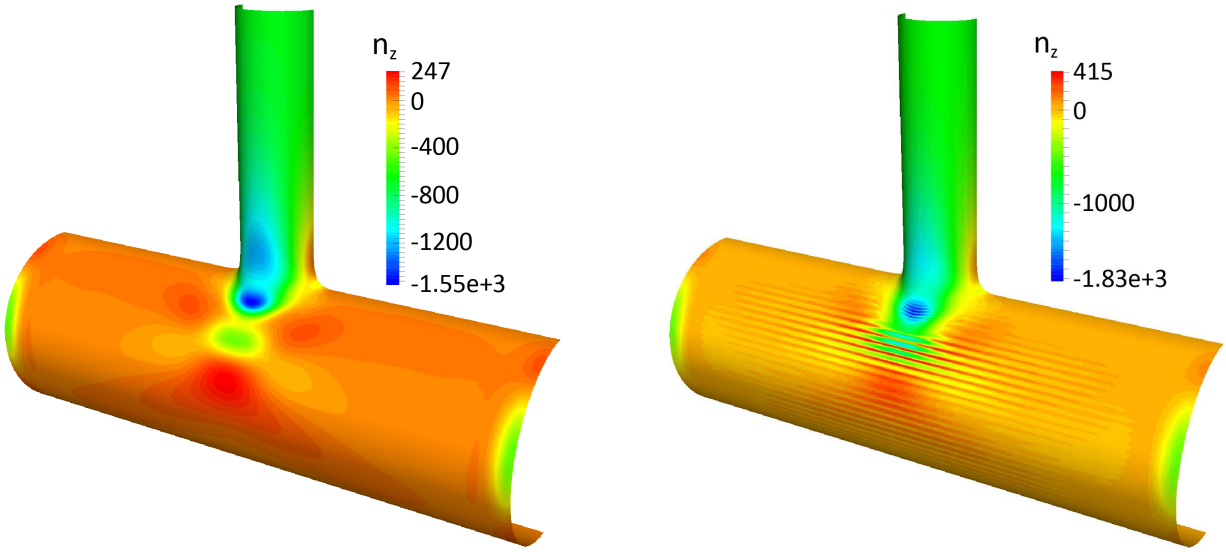

(a) (b)

Figure 22: Comparisons of stress resultant component n_z of the crossing tubes model with $p = q = 2$ and external load $8796.5N$: (a) isogeometric mixed Kirchhoff-Love shell model, (b) isogeometric single-field Kirchhoff-Love shell model.

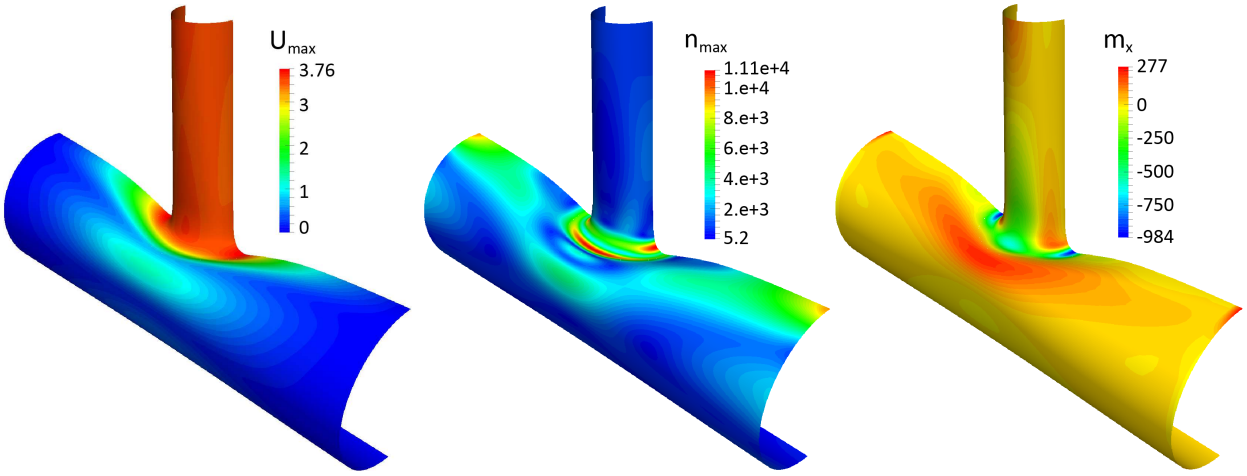

(a) (b) (c)

Figure 23: The post-buckling results of the multi-patch crossing tubes model ($p = q = 3$): (a) displacement field, (b) stress resultant, (c) bending moment.

5. Summary and conclusions

Despite a number of significant advancements in isogeometric thin-shell analysis, the issue of membrane locking in the context of non-linear multi-patch analyses remains an open problem in many aspects. Trimmed geometries, non-conforming patches, overlapping domains and the ele-

mental need for a continuity preserving coupling mechanism accross coupling interfaces are some of the most essential challenges to cope with. In this contribution, we addressed the aforementioned issues and proposed feasible solutions in order to provide a reliable and accurate analysis approach for models with relevance in the engineering routine. To this end, we have extended our isogeometric analysis framework by the following advancements: in a first step, we extended the Hellinger-Reissner thin-shell formulation of [11] from a pure linear theory to a non-linear theory considering large displacements. The theory is based on the assumptions of Kirchhoff-Love for thin shells comprising an independent strain interpolation to counteract membrane locking. In a second step, we equipped our implementation with the capability to handle properly trimmed domains in CAD-derived analysis models utilizing the principles of the finite cell method based on the recursive bi-section approach introduced in earlier publications. Herein, we have revisited the accuracy issue of our approach in order to judge on the overall solution quality of our method. A simple test example has confirmed a linear dependency of the integration accuracy on the computational effort spent for increasing refinement levels. The solution quality of the presented examples herein and experience values from previous works reinforce the potential of this algorithmic simple yet fail-safe and efficient approach to overcome the challenge of trimming.
Finally, we have derived a variationally consistent coupling formulation which ensures a discretization independent, continuity preserving and robust bond among different domains and trimmed patches. The presented coupling extension is new and unique in the context of a mixed thin-shell theory for geometric non-linear multi-patch analysis. Following the fundamental maxim of variational principles our coupling approach satisfies the necessary interface conditions in a weak sense and ensures a continuity preserving flux among the coupled domains. A critical comparison with the established penalty approach substantiated the superiority of our method with regard to several robustness aspects which we illustrated with problems of linear and non-linear elasticity. The penalty approach revealed severe shortcomings in terms of reliability and a strong dependency on the user-selected penalty value which is in conflict with the principle idea of this variationally inconsistent approach. In contrast, our Nitsche-like coupling approach applies a built-in stabilization which is self-adjusting to ensure optimal convergence properties. We tested our developments and extensions with a number of benchmark problems to reveal the performance properties. With a thin cylindrical shell strip, we studied the vulnerability to membrane locking for high slenderness degrees. A mixed shell penalty-based coupling and a pure single-field shell model showed some weakness or even a complete failure for increasing slenderness degrees. In contrast, the mixed shell Nitsche-type coupling convinced at all slenderness degrees without compromise. Similar results were observed for the Scordelis-Lo shell problem already for a quadratic approximation order. Severe oscillations in the shell's pressure zone were observed for the single field model indicating membrane locking, whereas the mixed formulation completely removed any disturbance of the elastic response showing completely smooth membrane forces with an excellent load transfer across the coupling interface between non-conforming patch discretizations. Again, the penalty-based coupling showed a similar unsteady load transfer along the coupling interface as the oscillating single-field solution does. A uniform h-refinement revealed for both models, single-field and mixed shell model, a convergence rate according to the approximation order.
In the context of large displacement analysis, we used a slit annular ring model to demonstrate the potential of the Nitsche-type mixed model with regard to the numerical stability of the method.

In comparison with a coupled single-field model, the load step size was increased by almost a factor 10 and the corresponding number of iterations needed to regain equilibrium was reduced by almost one order of magnitude. Hence, the proposed method shows a game-changing positive impact on the computational effort of the solution scheme. Moreover, it demonstrates the potential to outperform easily commercial finite element-based software on the basis of computational complexity and solution quality. Higher order continuity and a smooth solution field were retained for the mixed model all over including stress resultants and bending moments. Lastly, we considered a multi-patch model of crossing tubes to demonstrate the fitness of the proposed method for the engineering routine. The loaded tube design is prone to buckling and undergoes a distinct snap-through response. The complete equilibrium path was traced reliably within 10 load steps which is a fraction of the computational complexity required by a standard FEM analysis and which failed to converge in the post-buckling state. The single-field solution again suffered from oscillating membrane locking effects which were completely absent for the mixed shell, Nitsche-type coupled, Kirchhoff-Love model. The high robustness and improved performance properties of the method are clearly visible from this example which unifies all the critical issues of a CAD-derived analysis design which we addressed in this contribution. Moreover, a superior analysis result was demonstrated in all respects of linear and non-linear analysis.

Acknowledgments

Y. Guo would like to thank the National Natural Science Foundation of China (Grant no. 11972187, 11602106) and Natural Science Foundation of Jiangsu Province of China (Grant no. BK20160783) for their support.

Appendix A. Derivatives of the force vectors

In this appendix, we take the derivatives of the boundary forces with respect to the displacement and assumed membrane strain variables at an individual control point $\mathbf{B}_r$, instead of the total displacement $\mathbf{U}$ and membrane strain $\tilde{\boldsymbol{\epsilon}}$, since this will simplify many derivative expressions. To be more specific, we introduce the symbol $\mathbf{U}_r$ and $\tilde{\boldsymbol{\epsilon}}_r$ to represent the set of unknown displacement and membrane strain coefficients at the control point $\mathbf{B}_r$. We note that, the membrane strain variables are interpolated with lower order bases, therefore, the set of control points for the membrane strain field is different from that of the displacement field. For simplicity, we just use the same index for the two independent fields. We introduce a second control point index s when considering second order derivatives.

In eqs. (56) and (59), the first and second derivatives of the force vector w.r.t. the displacement and membrane strain variables reads:

$$\begin{aligned}
\frac{\partial\{\mathbf{F}\tilde{\mathbf{N}}^{\beta}\,\nu_{\beta}\}}{\partial(\mathbf{U}_r,\tilde{\boldsymbol{\epsilon}}_r)} &= \{\mathbf{F}\tilde{\mathbf{N}}^{\beta}\,\nu_{\beta}\}_{,\mathbf{U}_r}+\{\mathbf{F}\tilde{\mathbf{N}}^{\beta}\,\nu_{\beta}\}_{,\tilde{\boldsymbol{\epsilon}}_r}\\
&= \{\mathbf{F}_{,\mathbf{U}_r}\tilde{\mathbf{N}}^{\beta}\,\nu_{\beta}\}+\{\mathbf{F}\tilde{\mathbf{N}}^{\beta}_{,\mathbf{U}_r}\,\nu_{\beta}\}+\{\mathbf{F}\tilde{\mathbf{N}}^{\beta}_{,\tilde{\boldsymbol{\epsilon}}_r}\,\nu_{\beta}\} \qquad \text{(A.1)}\\
\frac{\partial^2\{\mathbf{F}\tilde{\mathbf{N}}^{\beta}\,\nu_{\beta}\}}{\partial(\mathbf{U}_r,\tilde{\boldsymbol{\epsilon}}_r)\,\partial(\mathbf{U}_s,\tilde{\boldsymbol{\epsilon}}_s)} &= \{\mathbf{F}\tilde{\mathbf{N}}^{\beta}\,\nu_{\beta}\}_{,\mathbf{U}_r\mathbf{U}_s}+\{\mathbf{F}\tilde{\mathbf{N}}^{\beta}\,\nu_{\beta}\}_{,\mathbf{U}_r\tilde{\boldsymbol{\epsilon}}_s}+\{\mathbf{F}\tilde{\mathbf{N}}^{\beta}\,\nu_{\beta}\}_{,\tilde{\boldsymbol{\epsilon}}_r\mathbf{U}_s}
\end{aligned}$$

$$
\begin{aligned}
&= \{\mathbf{F}_{,\mathbf{U}_r\mathbf{U}_s}\tilde{\mathbf{N}}^{\beta}\,\nu_\beta\} + \{\mathbf{F}_{,\mathbf{U}_r}\tilde{\mathbf{N}}^{\beta}_{,\mathbf{U}_s}\,\nu_\beta\} + \{\mathbf{F}_{,\mathbf{U}_s}\tilde{\mathbf{N}}^{\beta}_{,\mathbf{U}_r}\,\nu_\beta\} \\
&+ \{\mathbf{F}\tilde{\mathbf{N}}^{\beta}_{,\mathbf{U}_r\mathbf{U}_s}\,\nu_\beta\} + \{\mathbf{F}_{,\mathbf{U}_r}\tilde{\mathbf{N}}^{\beta}_{,\tilde{\boldsymbol{\epsilon}}_s}\,\nu_\beta\} + \{\mathbf{F}\tilde{\mathbf{N}}^{\beta}_{,\mathbf{U}_r\tilde{\boldsymbol{\epsilon}}_s}\,\nu_\beta\} \\
&+ \{\mathbf{F}_{,\mathbf{U}_s}\tilde{\mathbf{N}}^{\beta}_{,\tilde{\boldsymbol{\epsilon}}_r}\,\nu_\beta\} + \{\mathbf{F}\tilde{\mathbf{N}}^{\beta}_{,\tilde{\boldsymbol{\epsilon}}_r\mathbf{U}_s}\,\nu_\beta\} \qquad \text{(A.2)}
\end{aligned}
$$

where the following additional relations hold:

$$\mathbf{F}_{,\mathbf{U}_r} = \mathbf{a}_{\alpha,\mathbf{U}_r}\otimes\mathbf{A}^{\alpha} + \mathbf{d}_{,\mathbf{U}_r}\otimes\mathbf{D} \qquad \text{(A.3)}$$

$$\mathbf{F}_{,\mathbf{U}_r\mathbf{U}_s} = \mathbf{d}_{,\mathbf{U}_r\mathbf{U}_s}\otimes\mathbf{D} \qquad \text{(A.4)}$$

$$\tilde{\mathbf{N}}^{\beta}_{,\mathbf{U}_r} = \tilde{Q}^{\alpha\beta}_{,\mathbf{U}_r}\mathbf{A}_\alpha + \tilde{Q}^{\beta}_{,\mathbf{U}_r}\mathbf{D} \qquad \text{(A.5)}$$

$$\tilde{\mathbf{N}}^{\beta}_{,\mathbf{U}_r\mathbf{U}_s} = \tilde{Q}^{\alpha\beta}_{,\mathbf{U}_r\mathbf{U}_s}\mathbf{A}_\alpha + \tilde{Q}^{\beta}_{,\mathbf{U}_r\mathbf{U}_s}\mathbf{D} \qquad \text{(A.6)}$$

$$\tilde{\mathbf{N}}^{\beta}_{,\tilde{\boldsymbol{\epsilon}}_r} = \tilde{Q}^{\alpha\beta}_{,\tilde{\boldsymbol{\epsilon}}_r}\mathbf{A}_\alpha + \tilde{Q}^{\beta}_{,\tilde{\boldsymbol{\epsilon}}_r}\mathbf{D} \qquad \text{(A.7)}$$

$$\tilde{\mathbf{N}}^{\beta}_{,\mathbf{U}_r\tilde{\boldsymbol{\epsilon}}_s} = \tilde{Q}^{\beta}_{,\mathbf{U}_r\tilde{\boldsymbol{\epsilon}}_s}\mathbf{D} \qquad \text{(A.8)}$$

Following (42), the first and second derivatives of $\tilde{Q}^{\alpha\beta}$ reads:

$$\tilde{Q}^{\alpha\beta}_{,\mathbf{U}_r} = -b^{\alpha}_{\lambda,\mathbf{U}_r}\,M^{\lambda\beta} - b^{\alpha}_{\lambda}\,M^{\lambda\beta}_{,\mathbf{U}_r} \qquad \text{(A.9)}$$

$$\tilde{Q}^{\alpha\beta}_{,\tilde{\boldsymbol{\epsilon}}_r} = \tilde{N}^{\alpha\beta}_{,\tilde{\boldsymbol{\epsilon}}_r} \qquad \text{(A.10)}$$

$$\tilde{Q}^{\alpha\beta}_{,\mathbf{U}_r\mathbf{U}_s} = -b^{\alpha}_{\lambda,\mathbf{U}_r\mathbf{U}_s}\,M^{\lambda\beta} - b^{\alpha}_{\lambda,\mathbf{U}_r}\,M^{\lambda\beta}_{,\mathbf{U}_s} - b^{\alpha}_{\lambda,\mathbf{U}_s}\,M^{\lambda\beta}_{,\mathbf{U}_r} - b^{\alpha}_{\lambda}\,M^{\lambda\beta}_{,\mathbf{U}_r\mathbf{U}_s} \qquad \text{(A.11)}$$

where the derivatives of the mixed components of the surface's second fundamental form are defined as:

$$b^{\alpha}_{\lambda,\mathbf{U}_r} = a^{\alpha\beta}_{,\mathbf{U}_r}\,(\mathbf{a}_{\lambda,\beta}\cdot\mathbf{d}) + a^{\alpha\beta}\,(\mathbf{a}_{\lambda,\beta,\mathbf{U}_r}\cdot\mathbf{d} + \mathbf{a}_{\lambda,\beta}\cdot\mathbf{d}_{,\mathbf{U}_r}) \qquad \text{(A.12)}$$

$$
\begin{aligned}
b^{\alpha}_{\lambda,\mathbf{U}_r\mathbf{U}_s} &= a^{\alpha\beta}_{,\mathbf{U}_r\mathbf{U}_s}\,(\mathbf{a}_{\lambda,\beta}\cdot\mathbf{d}) + a^{\alpha\beta}_{,\mathbf{U}_r}\,(\mathbf{a}_{\lambda,\beta,\mathbf{U}_s}\cdot\mathbf{d} + \mathbf{a}_{\lambda,\beta}\cdot\mathbf{d}_{,\mathbf{U}_s}) \\
&+ a^{\alpha\beta}_{,\mathbf{U}_s}\,(\mathbf{a}_{\lambda,\beta,\mathbf{U}_r}\cdot\mathbf{d} + \mathbf{a}_{\lambda,\beta}\cdot\mathbf{a}_{3,\mathbf{U}_r}) \\
&+ a^{\alpha\beta}\,(\mathbf{a}_{\lambda,\beta,\mathbf{U}_r}\cdot\mathbf{d}_{,\mathbf{U}_s} + \mathbf{a}_{\lambda,\beta,\mathbf{U}_s}\cdot\mathbf{d}_{,\mathbf{U}_r} + \mathbf{a}_{\lambda,\beta}\cdot\mathbf{d}_{,\mathbf{U}_r\mathbf{U}_s}) \qquad \text{(A.13)}
\end{aligned}
$$

where the derivatives $a^{\alpha\beta}_{,\mathbf{U}_r}$ and $a^{\alpha\beta}_{,\mathbf{U}_r\mathbf{U}_s}$ can be derived from the relations $a^{\alpha\beta}\,a_{\beta\gamma} = \delta^{\alpha}_{\gamma}$ as:

$$a^{\alpha\beta}_{,\mathbf{U}_r} = -a^{\alpha\gamma}\,a_{\gamma\delta,\mathbf{U}_r}\,a^{\delta\beta} \qquad \text{(A.14)}$$

$$a^{\alpha\beta}_{,\mathbf{U}_r\mathbf{U}_s} = a^{\alpha\mu}\,a_{\mu\nu,\mathbf{U}_s}\,a^{\nu\gamma}\,a_{\gamma\delta,\mathbf{U}_r}\,a^{\delta\beta} - a^{\alpha\gamma}\,a_{\gamma\delta,\mathbf{U}_r\mathbf{U}_s}\,a^{\delta\beta} + a^{\alpha\gamma}\,a_{\gamma\delta,\mathbf{U}_r}\,a^{\delta\mu}\,a_{\mu\nu,\mathbf{U}_s}\,a^{\nu\beta} \qquad \text{(A.15)}$$

Following (43), the first and second derivatives of $\tilde{Q}^{\beta}$ reads:

$$\tilde{Q}^{\beta}_{,\mathbf{U}_r} = \left(M^{\alpha\beta}|_{\alpha}\right)_{,\mathbf{U}_r} + a^{\beta\gamma}\,(2\,\tilde{\varepsilon}_{\gamma\lambda}|_{\mu} - \tilde{\varepsilon}_{\lambda\mu}|_{\gamma})\;M^{\lambda\mu}_{,\mathbf{U}_r} + a^{\beta\gamma}_{,\mathbf{U}_r}\,(2\,\tilde{\varepsilon}_{\gamma\lambda}|_{\mu} - \tilde{\varepsilon}_{\lambda\mu}|_{\gamma})\;M^{\lambda\mu} \qquad \text{(A.16)}$$

$$\tilde{Q}^{\beta}_{,\tilde{\boldsymbol{\epsilon}}_r} = a^{\beta\gamma}\left(2\,(\tilde{\varepsilon}_{\gamma\lambda}|_{\mu})_{,\tilde{\boldsymbol{\epsilon}}_r} - (\tilde{\varepsilon}_{\lambda\mu}|_{\gamma})_{,\tilde{\boldsymbol{\epsilon}}_r}\right)\;M^{\lambda\mu} \qquad \text{(A.17)}$$

$$\tilde{Q}^{\beta}_{,\mathbf{U}_r\tilde{\boldsymbol{\epsilon}}_s} = a^{\beta\gamma}\left(2\,(\tilde{\varepsilon}_{\gamma\lambda}|_{\mu})_{,\tilde{\boldsymbol{\epsilon}}_s} - (\tilde{\varepsilon}_{\lambda\mu}|_{\gamma})_{,\tilde{\boldsymbol{\epsilon}}_s}\right) M^{\lambda\mu}_{,\mathbf{U}_r} + a^{\beta\gamma}_{,\mathbf{U}_r}\left(2\,(\tilde{\varepsilon}_{\gamma\lambda}|_{\mu})_{,\tilde{\boldsymbol{\epsilon}}_s} - (\tilde{\varepsilon}_{\lambda\mu}|_{\gamma})_{,\tilde{\boldsymbol{\epsilon}}_s}\right) M^{\lambda\mu} \tag{A.18}$$

$$\begin{aligned}\tilde{Q}^{\beta}_{,\mathbf{U}_r\mathbf{U}_s} &= \left(M^{\alpha\beta}|_{\alpha}\right)_{,\mathbf{U}_r\mathbf{U}_s} + a^{\beta\gamma}\,(2\,\tilde{\varepsilon}_{\gamma\lambda}|_{\mu} - \tilde{\varepsilon}_{\lambda\mu}|_{\gamma})\; M^{\lambda\mu}_{,\mathbf{U}_r\mathbf{U}_s} + a^{\beta\gamma}_{,\mathbf{U}_s}\,(2\,\tilde{\varepsilon}_{\gamma\lambda}|_{\mu} - \tilde{\varepsilon}_{\lambda\mu}|_{\gamma})\; M^{\lambda\mu}_{,\mathbf{U}_r} \\ &+ a^{\beta\gamma}_{,\mathbf{U}_r}\,(2\,\tilde{\varepsilon}_{\gamma\lambda}|_{\mu} - \tilde{\varepsilon}_{\lambda\mu}|_{\gamma})\; M^{\lambda\mu}_{,\mathbf{U}_s} + a^{\beta\gamma}_{,\mathbf{U}_r\mathbf{U}_s}\,(2\,\tilde{\varepsilon}_{\gamma\lambda}|_{\mu} - \tilde{\varepsilon}_{\lambda\mu}|_{\gamma})\; M^{\lambda\mu}\end{aligned} \tag{A.19}$$

where the terms $\left(M^{\alpha\beta}|_{\alpha}\right)_{,\mathbf{U}_r}$, $\left(M^{\alpha\beta}|_{\alpha}\right)_{,\mathbf{U}_r\mathbf{U}_s}$ and $(\tilde{\varepsilon}_{\gamma\lambda}|_{\mu})_{,\tilde{\boldsymbol{\epsilon}}_r}$ can be derived as:

$$\left(M^{\alpha\beta}|_{\alpha}\right)_{,\mathbf{U}_r} = M^{\alpha\beta}_{,\gamma,\mathbf{U}_r} + \Gamma^{\alpha}_{\lambda\gamma}\, M^{\lambda\beta}_{,\mathbf{U}_r} + \Gamma^{\beta}_{\lambda\gamma}\, M^{\alpha\lambda}_{,\mathbf{U}_r} \tag{A.20}$$

$$\left(M^{\alpha\beta}|_{\alpha}\right)_{,\mathbf{U}_r\mathbf{U}_s} = M^{\alpha\beta}_{,\gamma,\mathbf{U}_r\mathbf{U}_s} + \Gamma^{\alpha}_{\lambda\gamma}\, M^{\lambda\beta}_{,\mathbf{U}_r\mathbf{U}_s} + \Gamma^{\beta}_{\lambda\gamma}\, M^{\alpha\lambda}_{,\mathbf{U}_r\mathbf{U}_s} \tag{A.21}$$

$$(\tilde{\varepsilon}_{\gamma\lambda}|_{\mu})_{,\tilde{\boldsymbol{\epsilon}}_r} = \tilde{\varepsilon}_{\lambda\mu,\gamma,\tilde{\boldsymbol{\epsilon}}_r} - \Gamma^{\alpha}_{\lambda\gamma}\,\tilde{\varepsilon}_{\alpha\mu,\tilde{\boldsymbol{\epsilon}}_r} - \Gamma^{\alpha}_{\mu\gamma}\,\tilde{\varepsilon}_{\lambda\alpha,\tilde{\boldsymbol{\epsilon}}_r} \tag{A.22}$$

where the derivatives $M^{\alpha\beta}_{,\mathbf{U}_r}$, $M^{\alpha\beta}_{,\mathbf{U}_r\mathbf{U}_s}$, $M^{\alpha\beta}_{,\gamma,\mathbf{U}_r}$ and $M^{\alpha\beta}_{,\gamma,\mathbf{U}_r\mathbf{U}_s}$ can be derived from the constitutive relationship (34) and the definition of bending strains (22).

The derivatives of the membrane strain $\tilde{\varepsilon}_{\alpha\beta}$ and stress resultants $\tilde{N}^{\alpha\beta}$ in (A.10) and (A.22) are derived directly using the interpolation function (29) and the constitutive relationship (33). More details on relevant derivatives of the formulation can be found in [22].

References

[1] J. Kiendl, K.-U. Bletzinger, J. Linhard, and R. Wüchner. Isogeometric shell analysis with Kirchhoff-Love elements. *Computer Methods in Applied Mechanics and Engineering*, 198(49-52):3902–3914, 2009.

[2] T.J.R. Hughes, J.A. Cottrell, and Y. Bazilevs. Isogeometric analysis: CAD, finite elements, NURBS, exact geometry and mesh refinement. *Computer Methods in Applied Mechanics and Engineering*, 194:4135–4195, 2005.

[3] K.Y. Sze, W. Chan, and T. Pian. An eight-node hybrid-stress solid-shell element for geometric non-linear analysis of elastic shells. *Finite Elements in Analysis and Design*, 55(7):853–878, 2002.

[4] S. Klinkel, F. Gruttmann, and W. Wagner. A robust non-linear solid shell element based on a mixed variational formulation. *Computer Methods in Applied Mechanics and Engineering*, 195(1-3):179–201, 2006.

[5] M. Schwarze and S Reese. A reduced integration solid-shell finite element based on the EAS and the ANS concept—geometrically linear problems. *Computer Methods in Applied Mechanics and Engineering*, 80:1322–1355, 2009.

[6] K.Y. Sze and L. Yao. A hybrid stress ans solid-shell element and its generalization for smart structure modelling. part i - solid-shell element formulation. *International Journal for Numerical Methods in Engineering*, 48(4):545–564, 2000.

[7] M. Schwarze and S Reese. A reduced integration solid-shell finite element based on EAS and the ANS concept: Large deformation problems,. *International Journal for Numerical Methods in Engineering*, 85:289–329, 2011.

[8] Leonardo Leonetti and H. Nguyen-Xuan. A mixed edge-based smoothed solid-shell finite element method (mes-fem) for laminated shell structures. *Composite Structures*, 208:168 – 179, 2019.

[9] G.M. Kulikov, S.V. Plotnikova, and E. Carrera. Hybrid-Mixed Solid-Shell Element for Stress Analysis of Laminated Piezoelectric Shells through Higher-Order Theories. In H. Altenbach, E. Carrera, and G. Kulikov, editors, *Analysis and Modelling of Advanced Structures and Smart Systems. Advanced Structured Materials*, volume 81. Springer, Singapore, 2018.

[10] S. Klinkel, F. Gruttmann, and W. Wagner. *A robust nonlinear solid shell element based on a mixed variational formulation*, volume 2004(2) of *Mitteilungen, Institut für Baustatik*. Universität Karlsruhe, Karlsruhe, 2004.

[11] R. Echter, B. Oesterle, and M. Bischoff. A hierarchic family of isogeometric shell finite elements. *Computer Methods in Applied Mechanics and Engineering*, 254:170–180, 2013.
[12] M. Bischoff, W.A. Wall, K.U. Bletzinger, and E. Ramm. Models and finite elements for thin-walled structures. In E. Stein, R. de Borst, and T.J.R. Hughes, editors, *Encyclopedia of Computational Mechanics*, pages 59–137. John Wiley & Sons, Ltd., New York, 2004.
[13] E. Hellinger. Die allgemeinen Ansätze der Mechanik der Kontinuas. *Enzyklopdie der Mathematischen Wissenschaften*, 4/4:601–694, 1914.
[14] E. Reissner. On a variational theorem in elasticity. *Journal of Mathematical Physics*, 29:90–95, 1950.
[15] T.H.H. Pian and K. Sumihara. Rational approach for assumed stress finite elements. *International Journal for Numerical Methods in Engineering*, 20:1685–1695, 1984.
[16] D. Magisano, L. Leonetti, and G. Garcea. Advantages of the mixed format in geometrically nonlinear analysis of beams and shells using solid finite elements. *International Journal for Numerical Methods in Engineering*, 109(9):1237–1262, 2017.
[17] D. Magisano, K. Liang, G. Garcea, L. Leonetti, and M. Ruess. An efficient mixed variational reduced-order model formulation for nonlinear analyses of elastic shells. *International Journal for Numerical Methods in Engineering*, 113(4):634–655, 2018.
[18] D. Magisano, L. Leonetti, and G. Garcea. How to improve efficiency and robustness of the newton method in geometrically non-linear structural problem discretized via displacement-based finite elements. *Computer Methods in Applied Mechanics and Engineering*, 313:986–1005, 2017.
[19] R. Echter. *Isogeometric Analysis of Shells*. PhD thesis, Universität Stuttgart, Stuttgart, 2013.
[20] K. Rafetseder and W. Zulehner. A new mixed approach to kirchhoff–love shells. *Computer Methods in Applied Mechanics and Engineering*, 346:440–455, 2019.
[21] L. Wunderlich, A. Seitz, M.D. Alaydin, B. Wohlmuth, and A. Popp. Biorthogonal splines for optimal weak patch-coupling in isogeometric analysis with applications to finite deformation elasticity. *Computer Methods in Applied Mechanics and Engineering*, 346:197–215, 2019.
[22] Y. Guo, J. Heller, T.J.R. Hughes, M. Ruess, and D. Schillinger. Variationally consistent isogeometric analysis of trimmed thin shells at finite deformations, based on the step exchange format. *Computer Methods in Applied Mechanics and Engineering*, 336:39–79, 2018.
[23] A. Apostolatos, K.-U. Bletzinger, and R. Wüchner. Weak imposition of constraints for structural membranes in transient geometrically nonlinear isogeometric analysis on multipatch surfaces. *Computer Methods in Applied Mechanics and Engineering*, 350:938–994, 2019.
[24] Y. Guo, M. Ruess, and D. Schillinger. A parameter-free variational coupling approach for trimmed isogeometric thin shells. *Computational Mechanics*, 59:693–715, 2017.
[25] A. Apostolatos, R. Schmidt, R. Wüchner, and K.-U. Bletzinger. A Nitsche-type formulation and comparison of the most common domain decomposition methods in isogeometric analysis. *International Journal for Numerical Methods in Engineering*, 97:473–504, 2014.
[26] W. Dornisch, G. Vitucci, and S. Klinkel. The weak substitution method - an application of the mortar method for patch coupling in nurbs-based isogeometric analysis. *International Journal for Numerical Methods in Engineering*, 103(3):205–234, 2015.
[27] C. Hesch and P. Betsch. Isogeometric analysis and domain decomposition methods. *Computer Methods in Applied Mechanics and Engineering*, 213-216:104–112, 2012.
[28] M. Breitenberger, A. Apostolatos, B. Philipp, R. Wüchner, and K.-U. Bletzinger. Analysis in computer aided design: Nonlinear isogeometric B-Rep analysis of shell structures. *Computer Methods in Applied Mechanics and Engineering*, 284:401–457, 2015.
[29] Z. Lei, F. Gillot, and A. Jezequel. A C0 / G1 multiple patches connection method in isogeometric analysis. *Applied Mathematical Modelling*, 39(15):4405–4420, 2015.
[30] J. Kiendl, Y. Bazilevs, M.-C. Hsu, R. Wüchner, and K.-U. Bletzinger. The bending strip method for isogeometric analysis of Kirchhoff–Love shell structures comprised of multiple patches. *Computer Methods in Applied Mechanics and Engineering*, 199(37-40):2403–2416, 2010.
[31] D. Kamensky, J.A. Evans, M.-C. Hsu, and Y. Bazilevs. Projection-based stabilization of interface lagrange multipliers in immersogeometric fluid–thin structure interaction analysis, with application to heart valve modeling.

Computers & Mathematics with Applications, 74(9):2068–2088, 2017.

[32] K. Sommerwerk, Malte Woidt, Matthias Haupt, and Peter Horst. Reissner-mindlin shell implementation and energy conserving isogeometric multi-patch coupling: Iga shell implementation and multi-patch coupling. *International Journal for Numerical Methods in Engineering*, 109(7):982–1012, 2017.

[33] N. Nguyen-Thanh, K. Zhou, X. Zhuang, P. Areias, H. Nguyen-Xuan, Y. Bazilevs, and T. Rabczuk. Isogeometric analysis of large-deformation thin shells using RHT-splines for multiple-patch coupling. *Computer Methods in Applied Mechanics and Engineering*, 316:1157–1178, 2017.

[34] Y. Guo and M. Ruess. Nitsche's method for a coupling of isogeometric thin shells and blended shell structures. *Computer Methods in Applied Mechanics and Engineering*, 284:881–905, 2015.

[35] I. Harari and E. Grosu. A unified approach for embedded boundary conditions for fourth-order elliptic problems. *International Journal for Numerical Methods in Engineering*, 104(7):655–675, 2015.

[36] M. Ruess, D. Schillinger, A. I. Özcan, and E. Rank. Weak coupling for isogeometric analysis of non-matching and trimmed multi-patch geometries. *Computer Methods in Applied Mechanics and Engineering*, 269:46–71, 2014.

[37] V.P. Nguyen, P. Kerfriden, M. Brino, S.P. Bordas, and E. Bonisoli. Nitsche's method for two and three dimensional NURBS patch coupling. *Computational Mechanics*, 53(6):1163–1182, 2014.

[38] Y. Guo, H. Do, and M. Ruess. Isogeometric stability analysis of thin shells: from simple geometries to engineering models. *International Journal for Numerical Methods in Engineering*, 118:433–458, 2019.

[39] Y. Guo and M. Ruess. Weak Dirichlet boundary conditions for trimmed thin isogeometric shells. *Computers and Mathematics with Applications*, 70:1425–1440, 2015.

[40] D. Schillinger and M. Ruess. The finite cell method: A review in the context of higher-order structural analysis of cad and image-based geometric models. *Archives of Computational Methods in Engineering*, 22:391–455, 2015.

[41] A. Düster, J. Parvizian, Z. Yang, and E. Rank. The finite cell method for three-dimensional problems of solid mechanics. *Computer Methods in Applied Mechanics and Engineering*, 197:3768–3782, 2008.

[42] J. Parvizian, A. Düster, and E. Rank. Finite cell method - h- and p-extension for embedded domain problems in solid mechanics. *Computational Mechanics*, 41:121–133, 2007.

[43] J. Nitsche. Über ein Variationsprinzip zur Lösung von Dirichlet Problemen bei Verwendung von Teilräumen, die keinen Randbedingungen unterworfen sind. *Abhandlung aus dem Mathematischen Seminar der Universität Hamburg*, 36:9–15, 1970.

[44] Anita Hansbo and Peter Hansbo. An unfitted finite element method, based on Nitsche's method, for elliptic interface problems. *Computer Methods in Applied Mechanics and Engineering*, 191(47-48):5537–5552, 2002.

[45] P. Hansbo. Nitsche's method for interface problems in computational mechanics. *GAMM Mitteilungen*, 28/2:183–206, 2005.

[46] Roland Becker, Peter Hansbo, and Rolf Stenberg. A finite element method for domain decomposition with non-matching grids. *http://dx.doi.org/10.1051/m2an:2003023*, 37, 03 2003.

[47] A. Embar, J. Dolbow, and I. Harari. Imposing Dirichlet boundary conditions with Nitsche's method and spline-based finite elements. *International Journal for Numerical Methods in Engineering*, 83(7):877–898, 2010.

[48] M. Ruess, D. Schillinger, Y. Bazilevs, V. Varduhn, and E. Rank. Weakly enforced essential boundary conditions for NURBS-embedded and trimmed NURBS geometries on the basis of the finite cell method. *International Journal for Numerical Methods in Engineering*, 95:811–846, 2013.

[49] M. Hsu, D. Kamensky, Y. Bazilevs, M.S. Sacks, and T.J.R. Hughes. Fluid-structure interaction analysis of bioprosthetic heart valves: significance of arterial wall deformation. *Computational Mechanics*, 54:1055–1071, 2014.

[50] D. Schillinger, I. Harari, M.-C. Hsu, D. Kamensky, K.F.S. Stoter, Y. Yu, and Z. Ying. The nonsymmetric Nitsche method for the parameter-free imposition of weak boundary and coupling conditions in immersed finite elements. *Computer Methods in Applied Mechanics and Engineering*, 309:625–652, 2016.

[51] Y Bazilevs and T.J.R. Hughes. Weak imposition of Dirichlet boundary conditions in fluid mechanics. *Computers and Fluids*, 36:12–26, 2007.

[52] P.G. Ciarlet. An introduction to differential geometry with applications to elasticity. *Journal of Elasticity*, 78(1-3):1–215, 2005.

[53] B. Marussig and T.J.R. Hughes. A review of trimming in isogeometric analysis: Challenges, data exchange and simulation aspects. *Archives of Computational Methods in Engineering*, 25:1059–1127, 2018.
[54] H.-J. Kim, Y.-D. Seo, and S.-K. Youn. Isogeometric analysis for trimmed CAD surfaces. *Computer Methods in Applied Mechanics and Engineering*, 198:2982–2995, 2009.
[55] A. Stavrev. The role of higher-order geometry approximation and accurate quadrature in nurbs based immersed boundary method. Master's thesis, Technische Universität München, München, 2012.
[56] L. Kudela. Highly accurate subcell integration in the context of the finite cell method. Master's thesis, Technische Universität München, München, 2013.
[57] F. Cirak and Q. Long. Subdivision shells with exact boundary control and non-manifold geometry. *International Journal for Numerical Methods in Engineering*, 88(9):897–923, 2011.
[58] B. Jüttler, A. Mantzaflaris, R. Perl, and M. Rumpf. On numerical integration in isogeometric subdivision methods for PDEs on surfaces. *Computer Methods in Applied Mechanics and Engineering*, 302:131–146, 2016.
[59] A. Riffnaller-Schiefer, U.H. Augsdörfer, and D.W. Fellner. Isogeometric shell analysis with nurbs compatible subdivision surfaces. *Applied Mathematics and Computation*, 272,Part 1:139–147, 2016.
[60] T.W. Sederberg, J. Zheng, A. Bakenov, and A. Nasri. T-splines and T-NURCCs. *ACM Transactions on Graphics*, 22(3):477–484, 2003.
[61] Y. Bazilevs, V.M. Calo, J.A. Cottrell, J.A. Evans, T.J.R. Hughes, S. Lipton, M.A. Scott, and T.W. Sederberg. Isogeometric analysis using T-splines. *Computer Methods in Applied Mechanics and Engineering*, 199:229–263, 2010.
[62] D. Schillinger, M. Ruess, N. Zander, Y. Bazilevs, A. Düster, and E. Rank. Small and large deformation analysis with the p- and B-spline versions of the finite cell method. *Computational Mechanics*, 50:445–478, 2012.
[63] H. Kim, Y. Seo, and S. Youn. Isogeometric analysis with trimming technique for problems of arbitrary complex topology. *Computer Methods in Applied Mechanics and Engineering*, 199(45-48):2796–2812, 2010.
[64] László Kudela, Nils Zander, Tino Bog, Stefan Kollmannsberger, and Ernst Rank. Efficient and accurate numerical quadrature for immersed boundary methods. *Advanced Modeling and Simulation in Engineering Sciences*, 2, 06 2015.
[65] A.P. Nagy and D.J. Benson. On the numerical integration of trimmed isogeometric elements. *Computer Methods in Applied Mechanics and Engineering*, 284:165–185, 2015.
[66] J. A. Cottrell, T. J. R. Hughes, and Y. Bazilevs. *Isogeometric analysis: Towards Integration of CAD and FEM*. John Wiley & Sons, 2009.
[67] W. Pietraszkiewicz. Lagrangian description and incremental formulation in the non-linear theory of thin shells. *International Journal of Non-Linear Mechanics*, 19:115–140, 1983.
[68] S. Opoka and W. Pietraszkiewicz. Intrinsic equations for non-linear deformation and stability of thin elastic shells. *International Journal Solids and Structures*, 41:3275–3292, 2004.
[69] W. Jiang, C. Annavarapu, J. Dolbow, and I. Harari. A robust nitsche's formulation for interface problems with spline-based finite elements. *International Journal for Numerical Methods in Engineering*, 104:676–696, 2015.
[70] J.A. Evans and T.J.R. Hughes. Explicit trace inequalities for isogeometric analysis and parametric hexahedral finite elements. *Numerische Mathematik*, 123(2):259–290, 2013.
[71] P. Hansbo and M.G. Larson. Discontinuous Galerkin methods for incompressible and nearly incompressible elasticity by Nitsche's method. *Computer Methods in Applied Mechanics and Engineering*, 191(17-18):1895–1908, 2000.
[72] T. Belytschko, H. Stolarski, W.K. Liu, N. Carpenter, and J.S.-J. Ong. Stress projection for membrane and shear locking in shell finite elements. *Computer Methods in Applied Mechanics and Engineering*, 51:221–258, 1985.
[73] B. Oesterle, E. Ramm, and M. Bischoff. A shear deformable, rotation-free isogeometric shell formulation. *Computer Methods in Applied Mechanics and Engineering*, 307:235–255, 2016.
[74] B.A. Szabó and I. Babuška. *Finite element analysis*. John Wiley & Sons, 1991.
[75] K.Y. Sze, X.H. Liu, and S.H. Lo. Popular benchmark problems for geometric nonlinear analysis of shells. *Finite Elements in Analysis and Design*, 40:1551–1569, 2004.
[76] N. Buechter and E. Ramm. Shell theory versus degeneration – a comparison in large rotation finite element analysis. *International Journal for Numerical Methods in Engineering*, 34(1):39–59, 1992.
[77] Y. Başar and Y. Ding. Finite–rotation shell elements for the analysis of finite–rotation shell problems. *Interna-*

tional Journal for Numerical Methods in Engineering, 34(1):165–169, 1992.
[78] flexiCAD. *Rhinoceros — NURBS modeling for Windows*. http://www.de.rhino3d.com/, 2011.
[79] M. A. Crisfield. A fast incremental/iterative solution procedure that handles snap-through. *Computers & Structures*, 13:55–62, 1981.
[80] J. Bonet and R. Wood. *Nonlinear Continuum Mechanics for Finite Element Analysis*. Cambridge University Press, 2008.
[81] P. Wriggers. *Nonlinear Finite Element Methods*. Springer, Berlin, Heidelberg, 2008.
[82] Hibbit, Karlsson, and Sorensen. *ABAQUS/Standard Analysis User's Manual*. Hibbit, Karlsson, Sorensen Inc., USA, 2007.

View publication stats